CHALMERS UNIVERSITY OF TECHNOLOGY
Gothenburg, Sweden
www.chalmers.se

PHD THESIS

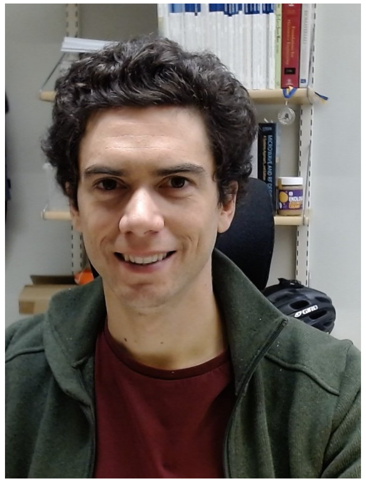

Microwave circuits are essential for applications such as radio astronomy, satellites, radars, atmosphere sensing, GPS, and wasting your time watching videos on your phone. Theoretically, the higher the frequency of the waves used, the more information you can send in communication links, the more resolution a radar can have, for example. Moreover, higher (terahertz) frequencies have other applications, such as security, medical applications, pharmaceutical quality control, and biological sensing. Unfortunately, present technology cannot generate as much power when frequency is increased. In addition, the chip loses a lot of power due to waves escaping the chip and metals absorbing more power. Without power, the signal quality deteriorates, like when you're in the middle of the forest with poor internet. For this reason, if we increase the frequency used in chips, it is important to minimise power losses to get the best signal quality. In my thesis, I researched a type of line which transports waves in chips (called planar Goubau line) which has relatively good power efficiency for terahertz waves, about 500 times higher frequency than most phones use nowadays. This planar Goubau line became trendy around the 2000s, and several researchers have already proposed some circuit components for filtering, for example. My contribution has been to propose the first calibration standard for this line so that it can be properly measured. I also suggested making the chips very thin, which prevents the waves from escaping the chip, decreasing the power losses. Apart from that, I designed several circuit components with an easy-to-tune design, including a filter (which lets some wave pass but not others), an absorber (to minimise reflections), and a power divider (which splits the power into two lines). Finally, I used the planar Goubau line to measure how terahertz waves change their power and velocity when they pass through a liquid sample, which could help microbiologists understand better the physics of proteins.

JUAN CABELLO SÁNCHEZ • Planar-Goubau-line components for terahertz applications • 2022

Planar-Goubau-line components for terahertz applications

JUAN CABELLO SÁNCHEZ

DEPARTMENT OF MICROTECHNOLOGY AND NANOSCIENCE - MC2
CHALMERS UNIVERSITY OF TECHNOLOGY
Gothenburg, Sweden 2022
www.chalmers.se

THESIS FOR THE DEGREE OF DOCTOR OF PHILOSOPHY

Planar-Goubau-line components for terahertz applications

Juan Cabello Sánchez

CHALMERS
UNIVERSITY OF TECHNOLOGY

Department of Microtechnology and Nanoscience - MC2
Chalmers University of Technology
Gothenburg, Sweden, 2022

Planar-Goubau-line components for terahertz applications

Juan Cabello Sánchez

Cover: visual metaphor of the thesis and its contents. Credit: Photoholgic.

ORCID: 0000-0002-9821-3199

ISBN: 978-91-7905-722-0
Doktorsavhandlingar vid Chalmers tekniska högskola, Ny series nr 5188
ISSN: 0346-718X
This thesis has been prepared using LaTeX.

Department of Microtechnology and Nanoscience - MC2
Chalmers University of Technology
SE-412 96 Gothenburg, Sweden
Phone: +46 (0)31 772 1000
`www.chalmers.se`

Printed by Chalmers Reproservice
Gothenburg, Sweden, October 2022

To grandpa Jesús, doctor in physics, who passed away the 4th of September 2017, at the start of my Ph.D. journey, who's curiosity, wisdom and transcendence continues to inspire me

It seems plain and self-evident, yet it needs to be said: the isolated knowledge obtained by a group of specialists in a narrow field has in itself no value whatsoever, but only in its synthesis with all the rest of knowledge and only inasmuch as it really contributes in this synthesis toward answering the demand, "Who are we?"— Erwin Schrödinger

If you wish to strive for peace of soul and happiness, then believe; if you wish to be a disciple of truth, then inquire.—Friedrich Nietzsche

The only true wisdom is in knowing you know nothing.—Socrates

The only certainty, it seems to me, is that those who believe they are certainly right are certainly wrong.— Iain McGilchrist

Abstract

Terahertz-wave technology has a broad range of applications, including radio astronomy, telecommunications, security, medical applications, pharmaceutical quality control, and biological sensing. However, the sources, detectors, and components are less efficient at this frequency band due to parasitic effects and increased total losses, which hinder the performance of terahertz systems. A common platform for terahertz systems is planar technology, which offers good integration, ease of fabrication, and low cost. However, it also suffers from high losses, which must be minimised to keep the system's performance. A pivotal choice to reduce losses is using power-efficient waveguides, and single-conductor waveguides have shown promisingly high power efficiencies compared to multi-conductor planar waveguides. The planar Goubau line (PGL) is a planar single-conductor waveguide consisting of a metal strip on top of a dielectric substrate which propagates a quasi-transverse magnetic surface wave, similarly to Sommerfeld's wire and the Goubau line, a conducting wire coated with a dielectric layer. Some limitations of the PGL, which complicate the design of components, are the lack of a ground plane and the weak dependence of impedance with the metal strip width of the line.

This thesis presents the development of PGL technology and components for terahertz frequencies. It developed design strategies to maximise the power efficiency, using electrically-thin substrates, which drastically drop radiation losses compared to thick substrates. The first PGL calibration standards were developed, which de-embeds the transition needed to excite the propagation mode and sets the calibration plane along the line, allowing the direct characterisation of PGL components. This work also presents several PGL components with a straightforward design procedure, including a stopband filter based on capacitively-coupled $\lambda/2$ resonators, an impedance-matched load based on an exponentially-tapered corrugated line, and a power divider based on capacitive-gap coupled lines to a standing wave in the input port. Finally, the PGL was integrated with a microfluidic channel to measure changes in the complex refractive index of a high-loss aqueous sample (water/isopropyl alcohol) as the first step toward a biological sensor.

Keywords: Impedance-matched load, microfluidic channels, on-wafer measurements, planar Goubau line, power divider, silicon membrane, stopband filter, terahertz spectroscopy, Through-Reflect-Line (TRL) calibration, vector network analyzers (VNA)

List of publications

The following appended papers constitute the main work for this thesis:

Paper A **J. Cabello-Sánchez**, H. Rodilla, V. Drakinskiy and J. Stake, "Multiline TRL Calibration Standards for S-parameter Measurement of Planar Goubau Lines from 0.75 THz to 1.1 THz," in proceedings of the *2018 IEEE/MTT-S International Microwave Symposium - IMS*, Philadelphia, PA, 2018, pp. 879-882, doi: 10.1109/MWSYM.2018.8439138.

Paper B **J. Cabello-Sánchez**, H. Rodilla, V. Drakinskiy, and J. Stake, “Transmission Loss in Coplanar Waveguide and Planar Goubau Line between 0.75 THz and 1.1 THz,” in proceedings of the *43rd International Conference on Infrared, Millimeter, and Terahertz Waves (IRMMW-THz)*, Nagoya, 2018, pp. 1–2, doi: 10.1109/IRMMW-THz.2018.8510326.

Paper C **J. Cabello-Sánchez**, V. Drakinskiy, J. Stake, and H. Rodilla, “Capacitively-coupled resonators for terahertz planar-Goubau-line filters,” accepted in *IEEE Transactions on Terahertz Science and Technology*, October 2022, doi: 10.1109/TTHZ.2022.3220599.

Paper D **J. Cabello-Sánchez**, V. Drakinskiy, J. Stake, and H. Rodilla, “A corrugated planar-Goubau-line termination for terahertz waves,” submitted to *IEEE Microwave and Wireless Components Letters*, November 2022, doi: 10.48550/arXiv.2210.11847.

Paper E **J. Cabello-Sánchez**, V. Drakinskiy, J. Stake, and H. Rodilla, “A capacitively-coupled power divider for planar Goubau line,” *manuscript*, October 2022.

Paper F **J. Cabello-Sanchez**, V. Drakinskiy, J. Stake and H. Rodilla, "On-Chip Characterization of High-Loss Liquids between 750 GHz and 1100 GHz," in *IEEE Transactions on Terahertz Science and Technology*, Vol. 11, No. 1, Jan. 2021, doi: 10.1109/TTHZ.2020.3029503.

Other papers and publications:

Paper I M. Jensen, V. Ahlberg Gagnér, **J. Cabello-Sánchez**, Å. Bengtsson, J.C. Ekström, T. Björg Úlfarsdóttir, M.J. Garcia-Bonete, A. Jurgilaitis, D. Kroon, V.T. Pham, S. Checcia, H. Coudert-Alteirac, S. Schewa, M. Rössle, H. Rodilla, J. Stake, V. Zhaunerchyk, J. Larsson and G. Katona, "High-resolution macromolecular crystallography at the FemtoMAX beamline with time-over-threshold photon detection," in *Journal of synchrotron radiation*, Vol. 28, No. 1, pp.64-70, doi: 10.1107/S1600577520014599

Paper II **J. Cabello-Sánchez**, V. Drakinskiy, J. Stake and H. Rodilla, “Terahertz Planar Goubau Line Components on Thin Suspended Silicon Substrate,” in proceedings of the *47th International Conference on Infrared, Millimeter, and Terahertz Waves (IRMMW-THz)*, Delft, 2022, pp. 1–2, doi: 10.1109/IRMMW-THz50927.2022.9896069.

Paper III M. Masyukov, I. Nefedova, A. Tamminen, K. Silvonen, **J. Cabello-Sánchez**, M. Varonen, M. Kantanen, H. Rodilla, J. Stake, Z. Taylor, “A calibration-free method to assess the quality of standards for THz on-wafer measurements,” in proceedings of the *47th International Conference on Infrared, Millimeter, and Terahertz Waves (IRMMW-THz)*, Delft, 2022, pp. 1–2, doi: 10.1109/IRMMW-THz50927.2022.9895704.

Paper IV V. Ahlberg Gagnér, M. Jensen, **J. Cabello-Sánchez**, Å. Bengtsson, J.C. Ekström, Z. Zhang, A. Jurgilaitis, D. Kroon, V.T. Pham, S. Checchia, H. Coudert-Alteirac, H. Rodilla, J. Stake, V. Zhaunerchyk, S. A. Mezzasalma, R. Friedman, J. Larsson and G. Katona, “Ultrafast structural response of a protein crystal to a strong pulsed THz field,” submitted to *Science Advances*, October 2022.

Acknowledgments

First and foremost, I would like to thank my main supervisor, **Helena**, for the guidance, support and fruitful and interesting discussions I've had with her. I loved brainstorming with you, trying to make sense of different research topics and fundamental questions, and chatting every now and then about random topics. Secondly, to my co-supervisor **Jan**, who has long-time expertise in the field, from which I learnt a lot about writing and publishing. A big thanks to **Vladimir**, who fabricated all my circuits and developed the processes, and from whom I learned so much about fabrication in general. Additionally, I enjoyed talking to him during fika breaks and exchanging different perspectives. Also, to **Mats** for micro-machining parts for my measurement setup. I was very often amazed by the ingenious designs of certain parts that I asked for. To our collaborators in the chemistry department at Chalmers, **Scott** and **Johan**, for the research we did together and for providing protein samples, gels, buffer and pumping equipment for challenging biological experiments that could not get published.

Thank you **Vessen** for always being helpful whenever there was some problem in the waveguide lab, for being opponent in my licentiate seminar and providing an interesting discussion; and crucially, for those fun lunch breaks and kite-surf sessions which would bring back the light and energy to this journey. To my dear French-viking friend, **Olivier**, who brought so many people together in his passage through Chalmers. It's always nice to have you around Chalmers and go for lunch breaks. I've learned many things from you, including how not to take life too seriously and, of course, kite-surfing, which has kept me alive in the last year. These two would help me keep my sanity and boost my research.

I feel grateful to **Anis** for sharing tips on measurements and post-processing and for proofreading my work. It was always nice to talk with you, share ideas and support each other. Thank you, **Divya**, for teaching me all the tricks on LaTeX(my figures look good thanks to your suggestion to use tikz), and for sharing your metrology experience, and measurements tricks (God bless those rectangular waveguide clamps!), and proofreading my work. **Isabel**, I want to thank you for being a supportive colleague and for being a role model for a hard-working PhD student. Your scholarship for a research visit to Stanford University helped inspire me to look more outside and aspire high. **Ahmed**, **Martin**, and **Frida**, for the good times going for lunch, beers, and whatnot; and Frida, once again, for throwing me out of my office when food called. To all my fellow PhD students at TML and MEL, **Marlene**, **Junjie**, **Yin**, **Marijana**, **Xinxin**, **Asad**, **Patrick**, **Ragnar**, **Han**, **Frida Olofsson**, **Göksu**, **Rob**, **Johan** etc. who made everyday life better inside and outside TML. It was

always interesting to talk to every one of you. I would like to thank **Johanna Hanning** for passing me her knowledge on THz measurements with VNA; you probably saved me months of getting started. **Serguei**, for always being happy to help with theory, experiments and finding equipment around the labs, in addition to testing our presentation skills by always asking tricky questions during Friday seminars. **Tomas**, for sharing your expertise and the fruitful discussions I had with you. **Andrei Vorobiev**, for the discussions regarding deep physics topics, when reading books did not yield answers. **Peter**, for being such a nice office mate at the beginning, for shining light on TML and for the nice discussions we had. **Stella Bevilacqua**, for sharing your experience at the beginning of the PhD. **Piotr Starski**, for your support regarding deep topics of microwave engineering. **Jörgen Stenarson**, for your support regarding the theory of calibration, your knowledge and tips saved me weeks of trial and error. **Anna Kim** and **Kiryl Kustanovich** for helping me with microfluidic channels at the start of my thesis. To the Gothenburg University microbiology research group, **Gergely**, **Majo**, **Viktor**, **Maja**, **Tinna**, for sharing long hours together during the syncrotron beamtimes in Hamburg and Lund.

I would like to give big thanks to my family, **mom**, **dad**, **Ana**, **Luis** and **Jaime** (I am who I am, greatly because of them). Seeing each other in Madrid was wonderful and fun. I feel lucky to have you all. My bike-loving flatmate **Lucas**, who is like a brother to me and helps me unwind every evening at home. To my dear friends **Mathias** and **Albert**, who I love spending time with and connect on so many levels. To my climbing friends (**Sabino**, **Eden**, **Francesco**, **Kayli**, etc.), who I spent so much time with in klätterlabbet and I'm glad to have met you all. To my **Spanish group** in Göteborg, who made me feel at home and was so refreshing to hang out with. To my old Politécnica de Madrid friends, **David**, **Ricardo**, **Jorge**, **Claudio**, **Luis**, for those amazing discussions and the motivation we got from each other. The fruits of our friendship still impact me today.

Other public figures who I've learnt a lot from and who have influenced me include Jordan Peterson, Iain McGuilchrist, Gabor Maté, Sam Harris, Robert Sapolsky, Antonio Escohotado, Noam Chomsky, Yuval Noah Harari, F. Nietzsche, A. Solzhenitsyn, Teresa of Ávila, Eckhart Tolle, Dale Carnegie, and Ben Felix, amongst others. And—why not—thank you to The Divine Presence, known and praised (in some way or another) in all cultures around the globe, which gives me gratitude, peaceful contentment, awe for everyday life, and serene hope.

This work was supported by the Swedish Research Council (Vetenskapsrådet) under grant 2015-03981 and 2020-05087, and Knut and Alice Wallenberg Foundation under grant 2014.0275.

Acronyms and abbreviations

CPW:	Coplanar Waveguide
DUT:	Device Under Test
PDMS:	Polydimethylsiloxane
PE:	Polyethene
PET:	Polyethylene-Terephthalate
PGL:	Planar Goubau Line
S-parameters:	Scattering parameters
SNR:	Signal-to-Noise Ratio
TE:	Transverse Electric
TEM:	Transverse Electromagnetic
THz:	Terahertz (1×10^{12} Hz)
TM:	Transverse Magnetic
TRL:	Through-Reflect-Line
VNA:	Vector Network Analyzer

Mathematical symbols

a	Wire radius
C	Capacitance
c	Speed of light in vacuum
d	Substrate thickness
$\vec{E}$	Electric field
E_t	Tangential electric field
E_z	Longitudinal electric field
E_ρ	Radial electric field in cylindrical coordinates
f	Frequency
f_c	Cutoff frequency
G	Conductance
$\vec{H}$	Magnetic field
H_t	Tangential magnetic field
H_z	Longitudinal magnetic field
H_ϕ	Azimuthal magnetic field in cylindrical coordinates
h_x	Radial decay constant
I	Current
J_c	Conduction current density
J_d	Displacement current density
J_α	Bessel function of the first kind of order α
j	Imaginary unit, $\sqrt{-1}$
K	Complete elliptic integral of first kind
K'	Complete elliptic integral of second kind
k_0	Wavenumber in vacuum
k_u	Wavenumber in periodic unit cell
L	Inductance
l	Length
l_c	Corrugation length
l_s	Sample length
l_u	Length of unit cell
$\tilde{n}$	Complex refractive index
n	Real refractive index
n_g	Real effective refractive index of guide
n_s	Real refractive index of substrate
P	Power
P'_c	Conductor power losses per unit length

P'_d	Dielectric power losses per unit length
R	Resistance
R_s	Surface resistance
$\vec{S}$	Poynting vector
S_{ij}	S-parameter from port$j$ to port$i$
s	Strip width (CPW and PGL)
t	Time
v_p	Phase velocity
w	Gap width (CPW)
X_i	Bessel or Hankel functions of the 1^{st} kind of order i
Y_p	Periodic admittance
Z_B	Characteristic impedance of periodically loaded waveguide
Z_c	Characteristic impedance
Z_{in}	Input impedance
Z_L	Load impedance
Z_{PI}	Power-current-defined characteristic impedance
z	Axial coordinate in cylindrical coordinates
$\vec{z}$	Cartesian and cylindrical coordinate vector. Propagation direction
α	Attenuation constant
α_c	Attenuation constant due to conductor loss
α_d	Attenuation constant due to dielectric loss
α_r	Attenuation constant due to radiation loss
β	Phase constant
γ	Propagation constant
γ_u	Propagation constant of unit cell
$\tan\delta$	Loss tangent, $(\epsilon''\omega + \sigma)/\epsilon'\omega$
$\tilde{\epsilon}$	Complex dielectric permittivity
ϵ'	Real part of dielectric permittivity
ϵ''	Imaginary part of dielectric permittivity
ϵ_0	Dielectric permittivity of vacuum
η	Intrinsic impedance
θ_r	Radiation angle
κ	Imaginary part of refractive index
λ	Wavelength
λ_0	Wavelength in vacuum
λ_d	Substrate wavelength, λ_0/n_s
λ_g	Guide wavelength, $\lambda_0/n_g = 2\pi/\beta$
μ	Magnetic permeability
μ_0	Magnetic permeability of vacuum
σ	Electrical conductivity

ϕ	Electrical length
$\hat{\phi}$	Cylindrical-coordinate vector
ω	Angular frequency

Contents

CHAPTER 1

Introduction

Terahertz (THz) waves, spanning between 0.3 THz and 10 THz in the electromagnetic spectrum, lie between the microwave and infrared bands. Traditionally, THz technology has been used in astronomy for detecting light-weight molecules [1], making this discipline a vital driver for THz technology in the early days. As new instrumentation was developed, the application of THz waves expanded to many other fields, including high-speed communications [2], pharmaceutical control [3], security [4], medicine [5], and biomolecular dynamics [6].

Terahertz components can be built in several technologies, including rectangular hollow waveguides [7], dielectric waveguides [8], and planar transmission lines [9]. Planar transmission lines consist of two or more flat conductors deposited on a dielectric substrate and have the advantages of good integration, ease of manufacturing and low cost. However, losses tend to increase at high frequencies, particularly radiation and ohmic losses. Therefore, it is paramount to minimise losses to have a high signal-to-noise ratio if this technology is used. Some of the most common metal planar waveguides used at THz frequencies are microstrip [10], coplanar waveguide [11], coplanar stripline [12], and planar Goubau line (PGL) [13]. Despite having a simple cross-section and a low attenuation constant, the PGL was relatively unexplored until the 2000s. The PGL consists of a metal strip on top of a dielectric substrate and propagates a quasi-transverse-magnetic (TM)—hybrid EH—surface wave [14]. Its field drops exponentially away in the transverse direction, similar to other surface waveguides [15], such as the Zenneck wave [16], [17], Sommerfeld wire [18], or the Goubau line [19], [20]. At low frequencies, the field extension of surface waveguides, such as the PGL, is physically large and can be impractical since it interacts with its surroundings. However, the field extension is reduced at higher frequencies, becoming practical, and the attenuation constant is low above 100 GHz [21], [22].

The propagation regime of the PGL mode depends on the electrical thickness of its substrate [23]. Electrically-thin substrates minimise radiation losses and dispersion and have demonstrated one of the highest power efficiencies for planar metal waveguides [24], thus being a good candidate to design circuit elements at THz frequencies. Some constraints of the PGL are that its characteristic impedance is weakly dependent on its strip width and lacks a ground plane. Both these characteristics complicated the design of circuit components, as opposed to other transmission lines. Nonetheless, some circuit elements have been designed for PGL, including stopband elements based on line corrugations [25], resonators [26]–[29], matched-loads [30]–[32], antennas [33]–[35], and power dividers [30], [31]. Table 1.1 shows the state-of-the-art in PGL circuit elements. However, most components have been designed and measured below sub-millimetre-wave frequencies, with a few exceptions passing 300 GHz [26], [28], [35], [36], which are shown **in bold** in Table 1.1. In addition, many of the components lack a straightforward design procedure. Moreover, the lack of calibration standards for PGL didn't allow direct measurements of the PGL, as it was not possible to de-embed the transitions used to excite the PGL mode.

This thesis has studied using the PGL as a planar waveguide at THz frequencies. **Paper A** proposes the first calibration standards developed for PGL, which de-embed the transition used to excite its surface wave and set the measurement reference plane along the PGL. **Paper B** shows how the PGL drastically reduces its attenuation constant by choosing an electrically-thin substrate which avoids leakage into other modes, demonstrating a higher power efficiency than a coplanar waveguide. This thesis also proposes several circuit components for PGL, which have a clear design procedure, unlike some of the hitherto proposed components. **Paper C** presents a stopband filter based on capacitively-coupled $\lambda/2$ resonators placed next to the PGL, with relatively low insertion losses. **Paper D** proposes an impedance-matched load based on an exponentially-corrugated PGL, which gradually increases conductor losses, and has a wideband operation with about 20 dB return loss, as good as the noise floor of our measurement setup. **Paper E** proposes a capacitively-coupled PGL power divider, which has a relatively wide bandwidth of operation, higher output power and isolation between output ports, and lower input-port reflections than T- and Y-shaped power dividers. Finally, the PGL was used for the spectroscopy of aqueous samples using microfluidic channels clamped on top of the substrate, obtaining similar sensitivity results from the ones presented for coplanar waveguide in **Paper F**.

Table 1.1: State-of-the-art in PGL components. Above 300 GHz **in bold**

Year	Circuit element	Meas. Freq. (GHz)	Reference
2006	Transition	140-220	[13]
2008	Microfluidic	0-220	[37]
2009	Corrugated PGL	140-220	[25]
2009	**Stub**	**0-1000**	**[26]**
2010	Filter	140-220	[27]
2011	Transition, load, pow.div.	40-65	[30]
2011	**Filter**	**200-325**	**[28]**
2012	Corrugated PGL	140-220	[38]
2012	**Pow. div., load**	**0-325**	**[31]**
2012	Microfluidic	50-110	[39]
2013	Resonators	140-220	[29]
2013	Antenna	37-41	[33]
2017	Corrugated PGL	2-10	[40]
2017	**Microfluidic**	**100-800**	**[36]**
2017	Antenna	4-7	[41]
2018	Antenna	5.4-6.6	[42]
2018	Filter	Simulations	[43]
2018	**Calibration standards**	**750-1100**	**Paper [A]**
2021	Corrugated PGL	250-300	[44]
2021	**Microfluidics**	**750-1100**	**Paper [F]**
2022	Filter	Simulations	[45]
2022	Resonator	Simulations	[46]
2022	Load	Simulations	[32]
2022	Antenna	7-40	[34]
2022	**Antenna**	**300-500**	**[35]**
2022	**Filter**	**500-1100**	**Paper [C]**
2022	**Load**	**500-1100**	**Paper [D]**
2022	**Power divider**	**500-1100**	**Paper [E]**

This thesis is structured as follows. Chapter 2 gives a theoretical background to the thesis, talking about transmission lines, surface waveguides, substrate modes, losses, characteristic impedance, and periodical structures. Chapter 3 explains the simulation environment used for the thesis and the design of the

PGL components and coplanar waveguide transition. Chapter 4 briefly describes the fabrication process of the chips designed on two different substrates, with a complete description available in Appendix A. Chapter 5 presents the measurement setup used to characterise the PGLs and components, together with results validating the PGL calibration standards, measurement of the proposed PGL components, and spectroscopy of high-loss aqueous samples using a PGL. Finally, chapter 6 finished with conclusions of the thesis and future outlook.

CHAPTER 2

Single-wire waveguides

This chapter gives a background for single-wire waveguides. The chapter starts presenting surface waveguides (Section 2.1), including the Sommerfeld line, Goubau line, and planar Goubau line—the waveguide studied in this thesis. It then lists some common planar transmission lines (Section 2.2) and gives an overview of the transmission line model (Section 2.3). Follows by substrate modes (Section 2.4), sources of losses in waveguides (Section 2.5), and finally, periodic structures and corrugations (Section 2.6).

2.1 Surface waveguides

Surface waveguides are structures which can support the propagation of surface waves. Surface waves [15], [47] are waves that can propagate at the interface between two media—dielectric-dielectric or dielectric-conductor—and are characterised to have a field which decays exponentially away from the interface.

Uller [16] and Zenneck [17] studied at the beginning of the 20^{th} century the TM surface waves propagating between two dielectric media with different permittivities. TM surface waves are possible when dielectric permittivity is different and the magnetic permeability is the same. By duality, transverse-electric (TE) surface waves are only possible when the permeabilities are different, with the same permittivities. TM surface waves require a boundary condition with an inductive surface impedance, whereas TE surface waves require a capacitive surface impedance [48].

In the case of surface waves propagating in metals, the characteristic impedance of metals is:

$$Z_m = \sqrt{\frac{j\omega\mu}{\sigma}}, \tag{2.1}$$

where $j = \sqrt{-1}$, ω is the angular frequency, μ the magnetic permeability, and σ is the conductivity. Then, finite-conductivity metals will present an inductive term; thus, TM modes surface waves are more relevant. A TM surface wave can propagate in the interface of a plane conductor and vacuum. Still, it will be too loosely bound to the surface, making it an unpractical waveguiding structure, as it will be prone to power leakage. To increase the field confinement to the metal, the surface reactance must increase without a major increase in the surface resistivity, which adds losses. This can be achieved by either coating the metal with a dielectric layer [19], [49] or by corrugating the surface of the metal [50]–[53]. If, on the contrary, the surface reactance tends to zero (a flat, perfect electric conductor), the surface wave will be poorly bound to the surface, and the longitudinal component of the electric field will be infinitely away from the surface, and the wave will have infinite power for a finite wave amplitude, similar to a plane wave.

The same principles can be applied to the case of a cylindrical metal. A single metal wire can propagate a TM surface wave as long as the surface impedance has an inductive term, and similarly, the inductive term can be increased with a layer of a dielectric material or by corrugating the wire. The main single-wire waveguides are the Sommerfeld line, the Goubau line, and the planar Goubau line, and they will be discussed in the following sections.

2.1.1 Sommerfeld line

In 1899 Sommerfeld described how a single conducting wire could propagate a TM surface wave [18] (Fig. 2.1a)—for an explanation in English from the same author, refer to sections 20 and 22 in [54]. The equations for the electric and magnetic field components travelling both inside and outside the conducting wire are, in cylindrical coordinates [20]:

$$E_z = AX_0(h_x\rho)e^{j(\omega t-\beta z)}, \tag{2.2a}$$

$$E_\rho = jA\frac{\beta}{h_x}X_1(h_x\rho)e^{j(\omega t-\beta z)}, \tag{2.2b}$$

$$H_\phi = jA\frac{k_x^2}{\omega\mu h_x}X_1(h_x\rho)e^{j(\omega t-\beta z)}, \tag{2.2c}$$

$$h_x = \sqrt{k_x^2 - \beta^2}, \tag{2.2d}$$

where inside the conducting wire ($0 \leq \rho \leq a$), the wavenumber $k_x = \sqrt{\omega\mu_c\sigma_c}e^{-j\pi/4}$ and outside ($a \leq \rho < \infty$), $k_x = \omega\sqrt{\epsilon\mu}$, A is a constant to be determined, h_x is a radial decay constant, ρ is the radial cylindrical coordinate, t is time, β is the phase constant, z is distance in the direction of propagation, and ϵ the dielectric permittivity. The cylindrical functions X_i are taken as Bessel functions of the first kind of order i inside the conductor and as Hankel functions of the first kind of order i outside the conductor. This TM wave is symmetrical around the axis of the wire, has an electric field which spreads radially from the metallic wire (Fig. 2.1b) and has no cut-off frequency. Naturally, the Sommerfeld line has many parallelisms to the surface wave propagating in a conducting plane [16], [17], and also requires an inductance term in the characteristic impedance of the metal wire to bind the surface wave to it. In the limit, when the radius of the wire is infinitely large, the solutions should converge with the case of the conducting plane. A detailed analysis of the Sommerfeld line can be found in [55], sections 9.16-17, where it covers the limit case when the Sommerfeld line has an infinite conductivity, and thus no surface reactance. As the conductivity increases, the $\vec{E}_z$ longitudinal component appears further away from the wire, being infinitely away for $\sigma \to \infty$. At this point, the mode becomes TEM, similar to a coaxial with conductors in infinity and with infinite power (similar to a plane wave), and thus, it is physically impossible.

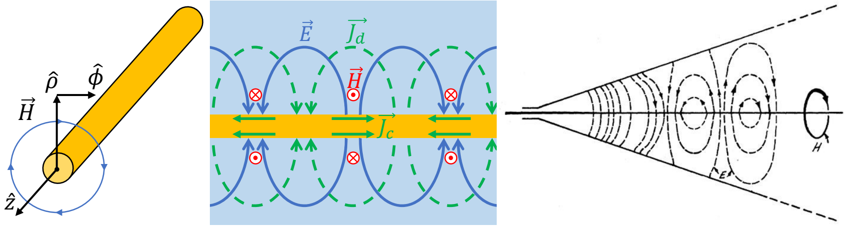

(a) **(b)** **(c)**

Figure 2.1: **(a)** Sketch of a Sommerfeld line and its transverse magnetic field. **(b)** Illustration of the side view of a Sommerfeld wire, showing the electric field, E, magnetic field, H, and conduction and displacement currents, J_c and J_d, respectively. **(c)** Mode-launching structure for a single-wire waveguide, as depicted in [56]. The coaxial's TEM mode is progressively converted into the TM mode, which propagates in the wire.

Despite needing to limit the conductivity of the wire to allow the propagation of waves, Sommerfeld's line has low attenuation constant and a phase velocity only a fraction smaller than c; however, it was never widely used since its extensive field (several metres for 1 GHz [20]) could be easily affected by nearby objects, since the wave is poorly bound to the metal wire.

The Sommerfeld surface wave needs to be launched by establishing the field distribution of its TM surface wave around the wire, which can be done with a coaxial line which gradually increases its outer conductor diameter progressively with a conical shape [56] (see Fig. 2.1.c). If this mode launcher does not replicate perfectly the field distribution of the surface wave (e.g. for having limited diameter), a supplementary radiating wave will be excited as well to satisfy the continuity of the field [56], decreasing the excitation efficiency. How about antennas with a single-wire feed? Do they propagate TM surface waves like the Sommerfeld wire? They don't since they lack the mode transition, which sets the TM surface wave field distribution and hence they mostly excite the radiating wave instead [56]. Additionally, the radiating wave is barely affected by the conductivity of the wire, unlike Sommerfeld's wire.

In 1959, Goubau pointed out how the nature of the propagation waves in metal wires was a controversial topic, in particular, if they intrinsically radiate power [57]. He suggested separating the propagating wave into a "truly guided" surface wave and a "partially-guided" radiating wave. These two waves must be orthogonal. Expressed mathematically:

$$\int_S (\vec{E}_S \times \vec{H}_R) n dS = \int_S (\vec{E}_R \times \vec{H}_S) n dS = 0 \tag{2.3}$$

where $\vec{E}_S$, $\vec{H}_S$ and $\vec{E}_R$, $\vec{H}_R$ are the field vectors of the surface wave and the radiating wave, respectively, and the integration is made in an equiphase surface of the surface wave. Goubau also pointed out that the excitation of a surface wave is always connected with the simultaneous excitation of a radiating wave, which can be minimised by correctly matching the field distribution of the mode converter. In [58], he implied that excitation of the Goubau line with a single dipole would give rise to both the surface and radiating wave, whereas a layer of properly distributed dipoles would excite the surface wave only. A possible explanation of why the TM surface wave does not radiate could come from its TM nature. The time-varying longitudinal electric field creates a displacement current, $\tilde{\varepsilon} d\vec{E}_z/dt$, in the direction of propagation, which has been suggested to be the return line for single-wire waveguides supporting TM surface waves [59], with the advantage that it does not suffer ohmic losses. According to Balanis [60], for radiation to occur, it is necessary to have a time-varying current or an accelerating charge. In the case where the displacement current is equal to the conducting current, the wire appears as current-neutral at a sufficiently long distance and thus does not radiate. This might explain why there are cases of published wires that experience radiation losses [61].

Sommerfeld's wire can support higher-order modes with a periodicity in the

$\hat{\phi}$ coordinate [62], but these asymmetric modes have most of the field inside the conductor and thus attenuate extremely fast [63], [64] due to ohmic losses ([54], pp.186). In addition, unlike the main TM propagating mode, these higher-order modes have cut-off frequencies below which they cannot propagate since their lateral wavenumber outside the conductor becomes zero, and thus the wave ceases to be bound to the wire, leaking the power.

To make the Sommerfeld line a more practical waveguide, the field needs to be more confined around the wire, a problem which can be solved by adding a dielectric layer, creating the Goubau line.

2.1.2 Goubau line

To increase the confinement of waves propagating in wires, Harms considered adding a dielectric layer to Sommerfeld's line [19] (Fig. 2.2), and the idea was further studied in detail by Goubau [20], [56]–[58], [65]. In almost all respects, the dielectric-coated wire, now commonly referred to as Goubau line, has the same properties as the Sommerfeld line. However, the higher confinement of the field in the Goubau allows it to propagate waves even when the metal wire has perfect conductance and makes it less susceptible to suffer radiation loss from bends in the waveguide compared to Sommerfeld's line, at the cost of an increase in ohmic losses [66]. Also, the increased field confinement makes mode-launching structures smaller and less prone to exciting radiating waves [57]. King et al. [21] reviewed the solutions for Sommerfeld and Goubau lines using more suitable approximations[1] for frequencies between 100 and 1000 GHz, and in 1961 [67] measurements were already made up to 140 GHz, showing an attenuation of 0.33 dB/m compared to more than 3.3 dB/m for rectangular waveguide.

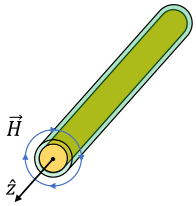

Figure 2.2: Sketch of Goubau line, whose field is more confined than in Sommerfeld's wire.

2.1.3 Planar Goubau line

The low-loss and ultra-wide bandwidth performance of single conducting waveguides impulsed the development of the planar Goubau line (PGL) [13], consisting of a metallic strip deposited on top of a dielectric substrate (Fig. 2.3a),

---

[1] Goubau assumed that $|\gamma a| \ll 1$ if the wire's radius, a is not too large. Whereas King assumed $J_0/J_1 \approx j$ if the radius is large compared to the skin depth, where J_α are Bessel functions of order α.

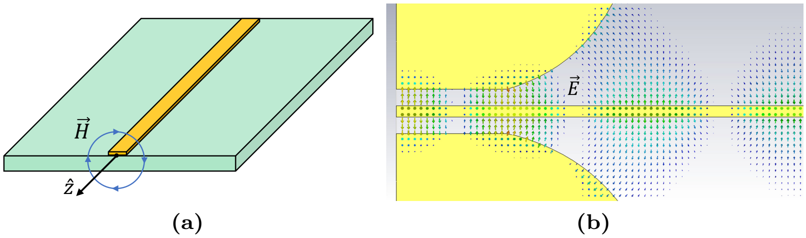

Figure 2.3: **(a)** Sketch of planar Goubau line where as a consequence of the higher permittivity of the substrate, the field is stronger on the substrate's side of the PGL. **(b)** Simulated electric field in the CPW-to-PGL mode converter, where the CPW's quasi-TEM mode is progressively converted into the PGL's quasi-TM mode.

which also has low loss and wideband characteristics. The term "planar Goubau line" was first used by [68] in 2004. For having such a simple cross-section, it is surprising that—to be the best of the author's knowledge—barely any studies were published in the 20th century on the propagation of surface waves in a metal strip on top of a substrate. In 1950 Coleman [69] studied the propagation of waves in a thin wire in between two media, but with no reference to surface waves. Others studied the diffraction caused by a metal strip to a plane wave in the boundary between two media [70] or the induced current in the strip [71]. Some researchers [72] found that the coplanar stripline's even mode propagated a surface wave whose propagation was not altered when both metals were united into a single strip—indirectly demonstrating the PGL. Propagation of surface waves along a metal strip in a homogenous medium was studied in [73] and in the boundary of two semi-infinite dielectrics [74].

Similarly to Sommerfeld's wire and the Goubau line, the PGL can propagate a surface wave, and instead of propagating a pure TM mode, it propagates a quasi-TM mode (or hybrid EH mode) due to its asymmetrical heterogeneous environment [14]. Unfortunately, many publications mention the planar Goubau line having a quasi-TEM mode [27]–[29], [38], [39], [75], [76] which, based on surface-wave theory, the author of this thesis humbly believes it's incorrect. The PGL mode decays exponentially perpendicular to the metal—as the Sommerfeld and Goubau lines—but also has a higher field concentration around the edges of the metal strip. Naturally, the electrical size of its substrate will influence the propagation regime of the surface wave, [23]. A thin substrate will produce phase velocities slightly below c for low enough frequencies, whereas at high enough frequencies, the field extension decreases and gets more confined in the substrate, lowering the phase velocity.

The PGL mode can be excited from another transmission line using a transition which gradually sets its field distribution. The most common transition used to launch the PGL mode is from CPW [75] (see Fig. 2.3b), although some transitions have been published for microstrip [30]. The CPW transition can be seen as the two-dimensional version of the metallic conical launching structure of Goubau's and Sommerfeld's waveguide. The PGL launcher starts as a three-conductor CPW and progressively separates the lateral ground strips to smoothly transform the coplanar waveguide's propagating even mode to the PGL's propagating mode, avoiding reflections and losses [77], [78] in the process.

Circuit components exist for PGL, increasing the applications it can be used for. However, most components have been designed and measured below sub-millimetre-wave frequencies, with a few being measured around 300 GHz [28], [31] and higher frequencies [26], [35], [36], which are shown in bold font in Table 1.1, in the Introduction section.

The PGL has been used for sensing [36], [37], [75] for its low-loss characteristics, negligible dispersion, wideband operation, good liquid sample deposition and large field extension, which allows it to sense larger volumes. However, these planar waveguides have never been demonstrated for sensing around 1 THz using vector network analysers due to a lack of available technology until recently.

2.2 Planar transmission lines

A transmission line is a waveguiding structure consisting of at least two conductors which have a constant cross-section perpendicular to the propagation direction. Having two or more conductors enables the propagation of TEM modes with no cut-off frequency and uniquely-defined voltages and currents. Some of the most common planar transmission lines include:

- Parallel-plate waveguide: it consists of two infinitely-long conducting planes sandwiching a dielectric material (Fig. 2.4.a). Since it has a homogeneous dielectric, a pure TEM mode can propagate inside of it without dispersion.

- Coplanar waveguide (CPW) [11]: it consists of three metal strips with a ground-signal-ground configuration on top of a dielectric substrate (Fig. 2.4.b). This transmission line has wideband characteristics, negligible dispersion, manageable losses at THz frequencies, high sensitivity to its near-field environment, and provides easy interfacing with ground-signal-ground probes. Its main propagation mode is the quasi-TEM even mode, which has a magnetic-plane symmetry across the centre line. An additional ground plane can be added in the backside of the substrate and is called a conductor-backed coplanar waveguide [79].

- Coplanar stripline [12]: similar to the coplanar waveguide, it consists of two metal strips on top of a dielectric substrate (Fig. 2.4.c). Its main propagation mode is the quasi-TEM odd mode, where there is an electric-plane symmetry in the gap between the strips. An even mode with magnetic-plane symmetry can also propagate and has the properties of a surface wave in a PGL [72]. In the case where the conducting strips are electrically wide, it is referred to as coplanar slotline [80].
- Microstrip [10]: it consists of a finite width conducting strip and a conducting plane sandwiching a dielectric material (Fig. 2.4.d), where most of the field lies between the two conductors. When the dielectric substrate is electrically small, the microstrip's propagating mode can be considered quasi-TEM with a certain effective permittivity. However, the inhomogeneous environment of the microstrip makes it a dispersive transmission line.

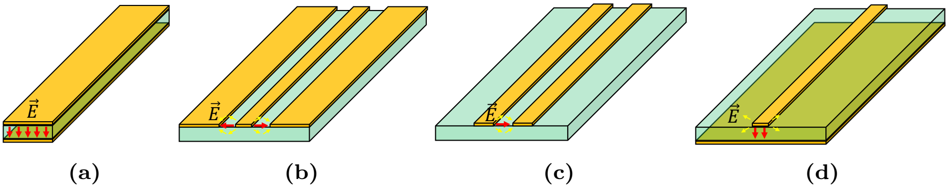

(a) **(b)** **(c)** **(d)**

Figure 2.4: Sketches of the planar transmission lines **(a)** parallel-plate waveguide, **(b)** coplanar waveguide, **(c)** coplanar stripline, and **(d)** microstrip, depicting the electric field of their main propagation mode. Orange colour is used to depict conductors, whereas green represents dielectrics.

2.3 Transmission-line theory

The transmission-line model [81]–[84] is a lumped-element electric circuit which describes the propagation of voltages and currents in an electrically-short transmission line. The model (shown in Fig. 2.5) has a series inductor, $L\,dz$, to account for the magnetic field around the conductors, and a shunt capacitance, $C\,dz$, to account for the displacement current flowing from the upper to the lower conductor. The series resistance, $R\,dz$, models the conductor losses, whereas the shunt conductance, $G\,dz$, models the dielectric loss. Then,

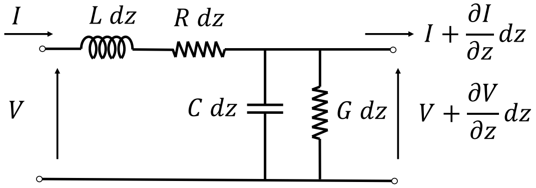

Figure 2.5: Equivalent circuit of a transmission line with an infinitesimal length.

the voltage and current waves propagating in the positive and negative direction of the $\hat{z}$-axis are:

$$V(z) = V^+ e^{-\gamma z} + V^- e^{\gamma z} \tag{2.4a}$$

$$I(z) = \frac{1}{Z_c}(V^+ e^{-\gamma z} - V^- e^{\gamma z}) \tag{2.4b}$$

where propagation constant, γ, and the characteristic impedance of the line, Z_c, are then given by:

$$\gamma = \alpha + j\beta = \sqrt{(R + j\omega L)(G + j\omega C)} \tag{2.5a}$$

$$Z_c = \sqrt{\frac{R + j\omega L}{G + j\omega C}} \tag{2.5b}$$

where γ describes how the magnitude and phase of the wave changes per unit length, whereas Z_c is the voltage-to-current complex ratio, in which if $GL = RC$, there is no phase difference between voltage and current.

In a lossless transmission line $R = G = 0$, and the following equation holds for $l \ll \lambda_g$ or $\phi = \beta l \ll 2\pi$:

$$L = \frac{Z_c n l}{c} = \frac{Z_c \phi}{\omega} \tag{2.6a}$$

$$C = \frac{nl}{Z_c c} = \frac{\phi}{Z_c \omega}. \tag{2.6b}$$

where n is the real effective refractive index of the transmission line, ϕ is its electrical length, l is the physical length, and λ_g is the wavelength in the transmission line.

The definition of characteristic impedance relates voltage-currents with electric-magnetic fields and needs to be power-consistent between the two domains. According to Schelkunoff [85], the characteristic impedance can be defined in several ways, and the definition choice does not matter as long as it is used consistently within a circuit. This thesis studied single-conductor waveguides in inhomogeneous media—planar Goubau lines—where the voltage difference between the conducting strip and infinity is not uniquely defined. For this reason, the impedance was defined based on power and current:

$$Z_{PI} = \frac{P}{|I|^2} = \frac{\int_A \vec{E} \times \vec{H}^* \, d\vec{A}}{\left| \oint_C \vec{H} \, d\vec{l} \right|^2}, \tag{2.7}$$

where the current was integrated around the conductor cross-section boundary, C, since displacement currents exist in the vicinity of the planar Goubau line, similarly to other single-conductor waveguides [59]. This definition of impedance has been used before for single-wire transmission lines [86]. In this thesis, this definition was equally applied to multi-conductor waveguides —like coplanar waveguide or coplanar stripline—where the current was defined by integrating the magnetic field in those conductors with a current in the direction of propagation of the wave. For example, for the coplanar stripline's odd mode, the current magnitude is that of a single metal strip, whereas, for the even mode, the current would be that of both strips.

2.4 Substrate modes

When the propagating mode in a planar transmission line has an effective refractive index, n_g, lower than the refractive index of an infinitely-thick substrate, n_s, it will produce radiating losses from the propagating mode in the transmission line to the substrate [87]. The wave will leak in the direction where both modes have a phase match [88], forming a radiation semi-cone with angle θ_r given by:

$$\cos\theta_r = n_g/n_s. \tag{2.8}$$

Note that in the case when $n_s < n_g$, there is no angle which satisfies the phase-matching condition between the two modes, and thus there won't be any leakage.

In finite-thickness substrates, surface waves can propagate, mainly the Zenneck modes (for conductor-backed dielectric sheets) and dielectric slab modes (for a dielectric sheet with no metal). For example, a transmission line with electrically large ground planes can be seen as a semi-grounded dielectric slab which can propagate a Zenneck wave [15], which are the same as the odd TE and even TM modes of an ungrounded dielectric slab of twice the thickness

[49]. The cut-off frequency of these surface modes is given by [48]:

$$\text{For TE}_m \text{ modes:} \quad f_c = \frac{m}{4d}\frac{c}{\sqrt{n_s^2-1}} \quad \text{where } m = 1, 3, 5, ... \tag{2.9a}$$

$$\text{For TM}_m \text{ modes:} \quad f_c = \frac{m}{4d}\frac{c}{\sqrt{n_s^2-1}} \quad \text{where } m = 0, 2, 4, ... \tag{2.9b}$$

where d is the thickness of the substrate. If the transmission line doesn't have a large metal plane, a TE_0 surface mode can propagate in the metal-less part of the substrate [89], increasing the possibilities for different types of parasitic mode excitation. In general, the cut-off frequency of the surface waves that can propagate in a ground-less dielectric slab is given by [90]:

$$\text{For TE}_m \text{ modes:} \quad f_c = \frac{m}{2d}\frac{c}{\sqrt{n_s^2-1}} \quad \text{where } m = 0, 1, 2, ... \tag{2.10a}$$

$$\text{For TM}_m \text{ modes:} \quad f_c = \frac{m}{2d}\frac{c}{\sqrt{n_s^2-1}} \quad \text{where } m = 0, 1, 2, ... \tag{2.10b}$$

The interaction between the transmission line's propagating mode with these surface waves depends on the overlap of their field distributions [91] and if they can satisfy a phase-matching condition, causing dispersion and radiation losses. This phenomenon is similar to what happens in an optical fibre, where the light will leak from the core if the refractive index of the cladding is higher than in the core. At the frequency where the phase velocity of the two waves is equal, the dispersion will be maximum, whereas the leakage losses are proportional to frequency [91]. To minimise these undesirable effects, the phase velocity of the substrate modes can be lowered, and the cut-off frequency of all modes can be multiplied by choosing an electrically-thin substrate [92]. A conservative rule-of-thumb is given in [91], where the substrate thickness is suggested to be taken as:

$$d < 0.12\lambda_0/n_s \tag{2.11}$$

Other suggested methods for reducing radiation losses include narrowing the conductors ($\lesssim \lambda/30$) [87], although conductor losses become too high at THz frequencies; adding a superstrate on top of the transmission line or adding corrugations [38], which would decrease the phase velocity, decreasing or stopping radiation losses to the substrate.

2.5 Losses in waveguides

The three sources of power loss in waveguides are dielectric, ohmic and radiation losses.

Dielectric losses are caused by dielectric materials which absorb the power of a wave, converting the power to heat. The expression for the attenuation constant due to dielectric losses is [93]:

$$\alpha_d = \frac{P_d'}{2P_t} = \frac{\frac{\sigma+\omega\epsilon''}{2}\displaystyle\int_A \left|\vec{E}\right|^2 dA}{2\displaystyle\int_A \langle\vec{S}\rangle\, d\vec{A}} \quad [\mathrm{Np/m}] \tag{2.12}$$

where P_t is the total power transported by the line, in the cross-section A covering all its field, P_d' is the power lost per unit length through dielectric losses, ϵ'' is the imaginary part of the dielectric permittivity, and $\vec{S}$ is the Poynting vector.

Ohmic losses are caused by finite-conducting materials posing resistance to the flow of electrons and absorbing the power of the wave. The equation for calculating the attenuation constant due to ohmic losses is [93]:

$$\alpha_c = \frac{P_c'}{2P_t} = \frac{\frac{R_s}{2}\displaystyle\int_A \left|\vec{H}_t\right|^2 dA}{2\displaystyle\int_A \langle\vec{S}\rangle\, d\vec{A}} \quad [\mathrm{Np/m}] \tag{2.13}$$

where P_c' is the power lost through ohmic losses per unit length, $R_s = \sqrt{\omega\mu/(2\sigma)}$ is the surface resistance, H_t is the magnetic field tangential to the conductor, and S is the surface area of the metal through a length of Δz. This equation holds accurate for $\eta = j\omega\mu/\gamma \ll \eta_0$, which for gold at 1 THz has $|\eta| \approx 0.0022\eta_0$, making it a good approximation. The ohmic losses are proportional to R_s, that is, proportional to $\sqrt{f}$, and naturally to the metal's properties $\sqrt{\mu/\sigma}$, which $\mu \gg 1$ for metals like iron and nickel. Also, the dielectric material around the metal can influence the conductor loss since dielectrics with higher permittivity will tend to concentrate the field.

Radiation losses are power leakage into other modes outside the waveguide. As seen in Section 2.4, the transmission line can leak power into another mode if a phase-matching condition can be satisfied [94], as well as having a non-orthogonal field distribution overlap [91]. This means that an open waveguide can radiate if its wave travels faster than other possible modes, including plane waves, dielectric slab modes, and other surface waves [94]. On a thick substrate, the power is radiated in a half cone towards the substrate, in a similar way to a shock wave [95], where the angle of radiation is given by eq. (2.8). The attenuation constant, α_r, from radiation losses from a CPW with a thick substrate gives an order of magnitude for radiation of planar waveguides. It is approximated by [96]:

$$\alpha_r = \left(\frac{\pi}{2}\right)^5 \frac{(1-1/n_s^2)^2}{\sqrt{2(1+1/n_s^2)}} \frac{(s+2w)^2}{\lambda_d^3 K(\zeta) K'(\zeta)} \tag{2.14}$$

where α_r is given in Neper per metre, s is the CPW's central strip width, w is the CPW's gap width, $\zeta = s/(s+2w)$, and K and K' are the complete elliptic integrals of the first and second kind, respectively. In [97], it gives approximations for power losses to TE and TM waves from a CPW (page 61) and a single narrow strip (page 63) in a thin substrate. Expressions are complex and need the context presented in the book, so the reader is referred to the book [97].

Some methods to reduce radiation are to increase β by adding a superstrate or corrugating the line, decreasing the phase constant of the allowed modes in the substrate, or reducing the substrate's thickness. More information about this type of radiation can be found in [87], [96].

2.6 Periodic structures

Periodic structures [98]—used in **Papers C and D**—are waveguides which are loaded at regular intervals with an identical impedance. They show a bandpass-stopband response and can support a wave with phase velocity much smaller than the speed of light [99]. These properties can be useful, amongst others, for the design of travelling-wave tubes, which amplify microwaves. Since the phase velocity is $v_p = (LC)^{-1/2}$, one could theoretically reduce the phase velocity by either increasing the inductance or capacitance of the transmission line in question. However, they are inversely proportional when the cross-section of the transmission line is constant. This can be solved by allowing the cross-section to vary periodically in the propagation direction, decreasing the capacitance without changing the inductance and, as a consequence, decreasing the phase velocity of the transmission line.

The waves travelling in the periodic waveguide are often referred to as Bloch waves. The periodic structure can be seen as a repeating unit cell. The ABCD matrix of a periodic unit cell can be built as a shunt element with a transmission line of length $l_u/2$ on each side (Fig. 2.6a). The result is:

$$\mathscr{A} = \cosh \gamma_u l_u + Y_p Z_c \sinh \gamma_u l_u, \tag{2.15a}$$

$$\mathscr{B} = Y_p Z_c^2 (\cosh \gamma_u l_u - 1) + Z_c \sinh \gamma_u l_u, \tag{2.15b}$$

$$\mathscr{C} = Y_p(\cosh \gamma_u l_u + 1) + \frac{1}{Z_c} \sinh \gamma_u l_u, \tag{2.15c}$$

$$\mathscr{D} = \mathscr{A}, \tag{2.15d}$$

where γ_u and Z_c are the propagation constant and characteristic impedance

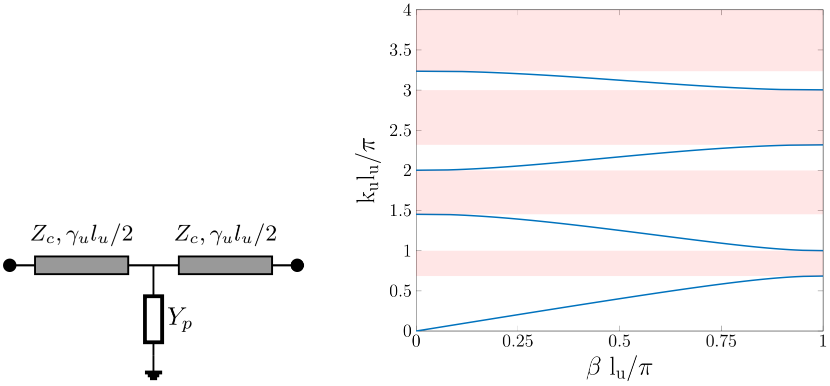

(a) **(b)**

Figure 2.6: (a) Transmission-line network of the unit cell of the periodic structure. **(b)** Example of a k-β diagram of a periodic structure with $Y_p = k_u l_u Z_c/2$, where the passbands are the values of $k_u l_u$ where a real value of β exist, and stopbands have been shadowed in red.

of the unloaded transmission line, and Y_p is the input admittance of the periodic shunt element. Assuming $l_u \ll \lambda_g$, the effective impedance of the periodically loaded transmission line is $Z_B = \sqrt{\mathscr{B}/\mathscr{C}}$. However, Z_B is not uniquely defined since it depends on the choice of periodic boundaries of the unit cell. The impedance of the periodic transmission line can be matched to a regular transmission line by tapering the shunt element throughout a length of λ_g, but a broadband matching will be challenging since Z_B has a frequency dependency.

A k-β diagram of a periodic structure (Fig. 2.6b) shows the pass- and stopbands, where there is a passband edge every time $k_u l_u$ is a multiple of π, where $k_u = \mathrm{Im}(\gamma_u)$. The group velocity will approach zero at each edge of the passbands except for when $k_u l_u = 0$.

2.6.1 Corrugated structures

Corrugations can be seen as a periodic structure in a waveguide, where the metal's dimension is varied perpendicular to the direction of propagation. Section 2.1.2 presented how a conducting wire could increase its surface reactance by applying a thin layer of dielectric material, increasing the confinement of the field in the Goubau line. An alternative method for changing the surface impedance of a conducting plane is by using corrugations. The corrugations in a conducting plane can be seen as parallel-plate waveguides, which are terminated in a short-circuit ($Z_L = 0$) [100]. The input impedance at the tip of the corrugations will then be:

$$Z_{in} = Z_c \frac{Z_L + jZ_c \tan\beta l_c}{Z_c + jZ_L \tan\beta l_c} = jZ_c \tan\beta l_c \tag{2.16}$$

where l_c is the corrugation length, and β is the phase constant in the corrugation. If $0 < \beta l_c < \pi/2$, the input impedance of the corrugated metal surface will increase its inductance term (supporting TM surface waves), and if $\pi/2 < \beta l_c < \pi$, it will have a capacitive term instead (supporting TE surface waves). Thus, corrugations will produce a frequency-periodic passband-stopband regime, where either TM or TE modes can propagate [51], where TM modes are more relevant since they propagate at lower βl_c. The increase of inductance from longer corrugations will increase the effective refractive index of the TM mode, its confinement to the metal and its conductor loss [50].

These properties can be used to increase the conductor losses to design low-reflective impedance-matched loads [32], [101]. Another possible application is to reduce radiation losses of a planar waveguide with an electrically-thick substrate [38] by increasing the phase constant of the waveguide above that of the substrate (see Section 2.5). Unfortunately, this method increases conductor loss since it induces more surface currents in the metal, and it is unlikely to decrease losses more than using electrically-thin substrates, especially at THz frequencies where conductor losses are higher. Sometimes corrugated waveguides are referred to in the literature as "spoof surface plasmon polariton waveguides" [102], taking their name from the highly-dispersive behaviour close to the corrugations cut-off frequency, whose propagation resembles surface plasmon waves naturally occurring at optical frequencies.

CHAPTER 3

Electromagnetic simulation and design of PGL components

This chapter describes in Section 3.1 the simulation environment used to analyse the developed waveguides and components presented in this thesis, including a description of the PGL simulation port used to excite the PGL without needing a CPW-to-PGL transition. Section 3.2 explains the criteria for the choice of substrate and presents the two substrates used in this thesis. Finally, Section 3.3 explains the design considerations for CPWs and PGLs and the impact of different parameters.

3.1 Electromagnetic simulations

This thesis ran 3D electromagnetic simulations in CST Studio Suite® using the "time-domain solver" (based on finite-integration technique method [103]) for the design of the CPW and PGL structures, and to contrast results with measurements. The "time-domain solver" has the advantage of being efficient for elements without a strong resonance, such as transmission lines, filters and antennas. The "time-domain solver" was compared with the "frequency-domain solver" (based on the finite-element method [104]) and the "multilayer solver" (based on the method of moments), but for our case, they were more time-consuming without added accuracy. All simulated materials accounted for conductor and dielectric loss, and their parameters were taken from the literature. The simulated circuit elements were excited using waveguide ports. Simulation trials using discrete and lumped-element ports did not succeed in correctly exciting the PGL. The simulation environment had "open" (absorbing) boundary conditions in its contour so radiated waves could exit the simulation environment without causing reflections. The "open (add space)" boundary was used when simulated structures were too close to the boundary edges. The boundary conditions for the port's plane were taken as an "electric" ($E_t = 0$) or "magnetic" ($H_t = 0$) boundary to force the electric field to be perpendicular or parallel to the port edge, respectively. Using open boundary conditions forces a parallel electric field in the port edges, similarly to the magnetic boundary. Regarding the mesh, the impact of increasing mesh density in simulation results was studied, showing that the default mesh settings produced convergent results. The mesh type chosen was hexahedral, with an accuracy of -40 dB, which was changed to -80 dB when circuit elements had very low levels of S_{11} or S_{21}. For wideband simulations, the "Inhomogeneous port accuracy enhancement" option was used, as otherwise, the port would be adapted for a certain frequency range, showing a lower magnitude of the transmission on the side of the simulated bandwidth. The waveguide in contact with the port kept its cross-section constant in the direction of propagation for a minimum length equal to the 40-dB-attenuation length of higher-order modes, avoiding a significant power of the evanescent modes to return to the port. Whenever possible, the electric and magnetic symmetry planes were used, as well as reciprocity and port symmetries, to decrease simulation time.

Other electromagnetic simulation software were explored for comparing results, in particular Ansys® Electronic Desktop (HFSS), based on finite-element method. The conclusion was that unlike CST Studio Suite®, it could not excite the PGL mode using a "wave port" or "lumped port", exciting other hybrid higher-order modes instead. The excitation of the PGL mode using CST Studio Suite® is discussed in the following section. However, COMSOL Multiphysics®, based on the finite-element method, was used to numerically calculate the impedances and phase velocities of the waveguides used since it allowed complete control of their definition.

3.1.1 Simulation of PGL port

The possibility of exciting the PGL directly, without needing an intermediate CPW-to-PGL mode transformer, would reduce simulation time and provide a better simulation environment for future analysis/synthesis of PGL elements.

The simulated PGL was excited with a square wave port centred around its conducting strip. Since the wave port has perfect conducting edges, the excited mode can be seen as a square coaxial-line mode. In [56] Goubau explains

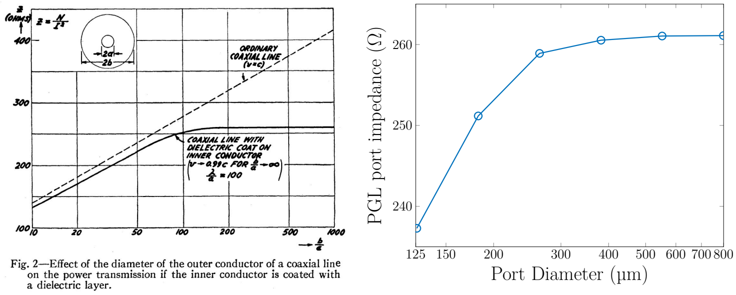

Fig. 2—Effect of the diameter of the outer conductor of a coaxial line on the power transmission if the inner conductor is coated with a dielectric layer.

(a) **(b)**

Figure 3.1: Simulated PGL port impedance is coherent with theory. (a) Figure taken from [56] depicting the impedance of coaxial with dielectric coating in inner conductor. **(b)** Simulated PGL port impedance vs square port size, showing similar behaviour as Goubau's results.

how a coaxial with an inner conductor coated in dielectric causes the field to have a longitudinal electric component. If the outer conductor radius of the coaxial is increased, there is a point where it no longer changes the field distribution around the inner conductor. As a consequence, the characteristic impedance's value of the dielectric-coated coaxial saturates after a certain outer conductor radius, unlike the uncoated coaxial's impedance which continues to increase logarithmically (Fig. 3.1.a). Since the PGL has a similar TM mode to the Goubau line, these results suggest that for a sufficiently large wave

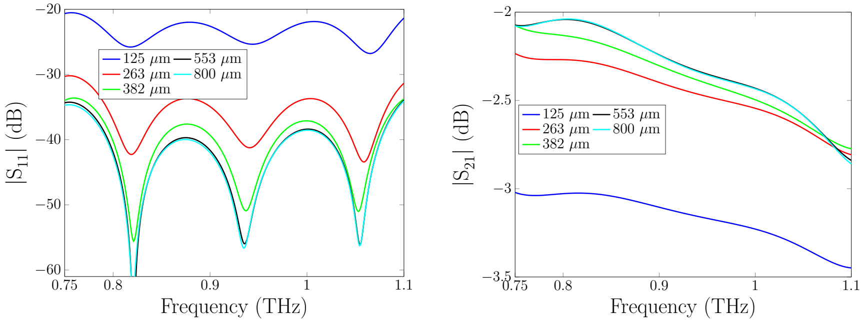

(a) **(b)**

Figure 3.2: Simulation results using PGL port converge for sufficiently large PGL port size. CST simulation results of **(a)** S_{11} and **(b)** S_{21} of a 3-mm-long PGL on a 30-µm-thick benzocyclobutene substrate for different port sizes.

port, both the S-parameter results and the impedance value should converge. Indeed, simulation results (Fig. 3.1.b) show that the port impedance saturated for increasing port size, similarly to Goubau's results. Similarly, S-parameter simulations results also converged for increasing port size (Fig. 3.2). Thus the port size was taken as the smallest size, which yielded convergent simulated S-parameter results, with 800 µm sides in a square wave-port, around 2λ.

3.2 Choice of substrate

THz planar waveguides must be designed to minimise the high losses occurring at THz frequencies to maximise the measurement signal-to-noise ratio (SNR). The main source of losses in planar structures is conductor and radiation losses if the substrate material is chosen with sufficiently-low dielectric losses. Apart from having low dielectric losses, an electrically-thin substrate is key for minimising radiation losses, as seen in seen Section 2.4 and 2.5. Fig. 3.3a shows the power leakage of a thick substrate compared to a thin one. In the course of the thesis, two electrically-thin substrates were used: a 23-µm-thick ($\sim 0.14\lambda_0/n_s$) polyethene-terephthalate (PET) film, and a 10-µm-thick high-resistivity silicon membrane ($\sim 0.11\lambda_0/n_s$) fabricated on a silicon-on-insulator wafer.

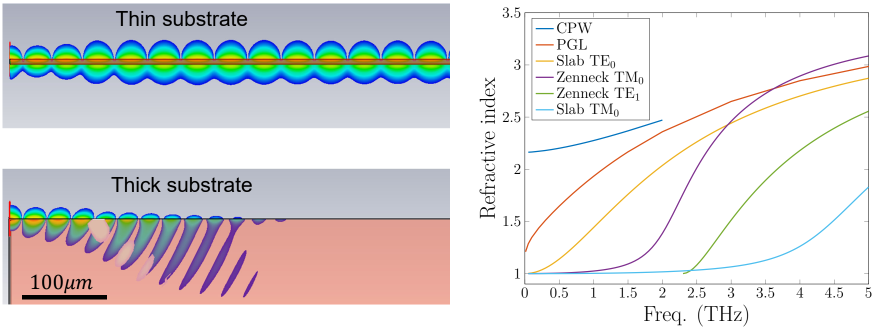

(a) **(b)**

Figure 3.3: **(a)** Side view of the wave propagation in a PGL at 1 THz with thin (10-µm-thick) and thick (semi-infinite) silicon substrate (in red). The thick substrate produces power leakage from the PGL. **(b)** Refractive index vs. frequency for CPW, PGL and substrate modes for the 10-µm-thick silicon membrane. Power leakage can occur when the refractive index is lower than that of the substrate modes.

Plastics usually have very low losses at THz frequencies [105] and have a low dielectric constant, which makes them ideal for having a low-loss and electrically-thin substrate. Some plastics cannot handle the high temperatures (100 °C) required in the chip's fabrication process, so a plastic with good electrical properties was chosen while having a relatively high melting point and mechanical strength. Considering this, a 23-µm-thick PET film (Mylar® A, fabricated by DuPont) was chosen as substrate, which was modeled in simulations with a relative permittivity of $\epsilon' = 3.15$ and $\tan(\delta) = 0.017$ around 1 THz [105]. For the substrate to be electrically-thin for the transmission line, the plastic-film substrate needs to be suspended in air, which was done by placing it on a supporting substrate with cavities under the transmission lines, which required careful alignment.

The silicon membrane substrate had the advantage of not requiring aligning with the supporting substrate. Instead, the bulk silicon of the chip was removed from below the transmission lines in the fabrication process, making the devices suspended completely in the membrane, having air below. The relative permittivity of high-resistivity silicon was modeled in simulations with a relative permittivity of $\epsilon' = 11.7$ and $\tan(\delta) = 1.7 \cdot 10^{-5}$ around 1 THz according to [106].

Fig. 3.3b shows the refractive index vs frequency for CPW, PGL and substrate modes for the 10-µm-thick silicon membrane substrate, simulated in COMSOL. The CPW has a 10-µm strip width and 15 µm gap, and the PGL has a 10-µm strip width. Both CPW and PGL have a higher refractive index than the substrate modes for frequencies considered in this thesis, below 1.1 THz, and therefore won't suffer from leakage to these modes. Zenneck modes arise only on metal planes with dielectric, in this case, CPWs with large ground planes, whereas slab modes appear on ungrounded dielectric slabs. The CPW is simulated up to 2 THz since, at higher frequencies, hybrid modes would be excited.

3.3 Design of planar waveguides

Different waveguides have different attenuation constants. Fig. 3.4 shows an example of simulation results of the attenuation constant of several types of planar waveguides using the same 10-µm-thick high-resistivity silicon substrate and using the same strip width and separation between metals of 10 µm. In this case, the PGL and CPW show lower simulated losses.

This thesis used PGL and CPW based on several reasons: they have the maximum field at the top, accessible to possible spectroscopy of samples; their easy fabrication and measurement with ground-signal-ground probes and their relative low-losses compared to other planar waveguides, as is shown in Fig. 3.4.

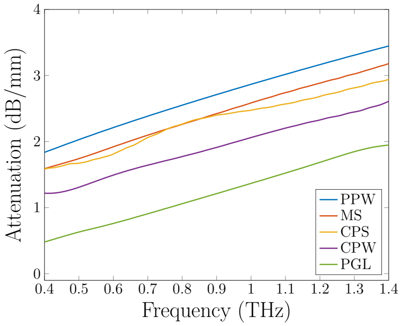

Figure 3.4: The PGL shows to have the lowest simulated attenuation constant in a 10-µm-thick silicon membrane. Simulated attenuation constant of different transmission lines in the same substrate and using the same conductor width and gap dimensions, 10 µm. PPW: parallel-plate waveguide. MS: microstrip. CPS: coplanar stripline (odd mode). CPW: coplanar waveguide (even mode). PGL: planar Goubau line.

3.3.1 Coplanar waveguide

The CPWs presented in this thesis were designed to have low losses [107] and to be suitable for probing with ground-signal-ground probes [108]. The main design parameters of the CPW are its strip-, gap-, and ground plane width and the substrate's material and thickness. The strip, s, and gap, w, widths were designed to have the centre of the CPW gaps between the centre of the probe tips for better probing alignment, having the sum $s + w$ equal to the probe pitch, 25 µm. The degree of freedom for the CPW dimensions was solved with two strategies. The first, having the same characteristic impedance as the probe, 50 Ω, minimising reflections, yielding $s = 23.5$ µm and $w = 1.5$ µm for the PET substrate (see Fig. 3.5a and Fig. 3.8a). The second, minimising loss by avoiding small s and w values, choosing $s = 10$ µm and $w = 15$ µm (see Fig. 3.5b and Fig. 3.7a). This second strategy resulted in higher delivered power and thus was preferred. Ground planes were chosen to be electrically big, although it has been reported that it increases radiation losses [109]. With an infinite ground plane, the surface wave with the lowest cut-off frequency is a Zenneck TM_0 mode, eq. (2.9b), whereas with a finite ground plane it is a dielectric slab TE_0 mode, eq. (2.10a). The CPW will leak to these modes when its phase velocity becomes higher than those of the substrate modes.

Multi-tine Through-Reflect-Line (TRL) calibration standards were also designed for CPW and fabricated and integrated into the devices' chip. The Through standard has a total length of 210 µm, placing the calibration plane at its mid-point, 105 µm from the start of the CPW. The Line standards were

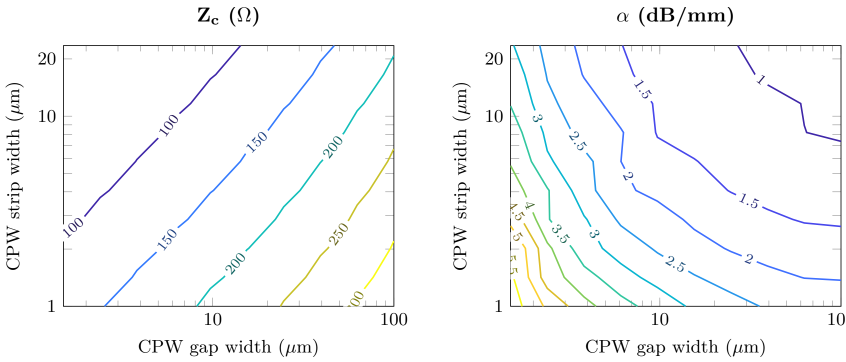

(a) **(b)**

Figure 3.5: **(a)** Characteristic impedance and **(b)** attenuation constant in dB/mm of a simulated CPW on a 23-µm-thick PET substrate as a function of the CPW strip width and gap. CPWs with wider strips and gaps show lower simulated attenuation. The characteristic impedance is proportional to the gap size and inversely proportional to the strip width.

designed with electrical lengths of $\lambda_g/4$, $3\lambda_g/4$, and $11\lambda_g/4$ at the centre of the measured band, 910 GHz.

3.3.2 Planar Goubau line

Simulation results indicate that the PGL radiation losses are proportional to the substrate's thickness [87], as it can be seen in Fig. 3.6a; therefore, it is key to choose an electrically-thin substrate. Once an electrically-thin substrate is chosen, the only design parameter of a PGL is the strip width. An increase in strip width decreases both the characteristic impedance of the PGL and its effective refractive index, according to simulations (Fig. 3.6b). However, the impedance has a weak dependence with strip width, so changing the width has limited applications. The attenuation constant due to conductor loss are also inversely proportional to the strip width. Therefore a reasonably wide 10-µm strip was chosen.

The PGL can be excited with ground-signal-ground probes using a CPW-to-PGL mode converter (Fig. 3.7a and Section 2.1.3). The probes contact the CPW section in the converter, exciting the CPW's quasi-TEM even mode, which is then converted into the PGL's TM mode. This mode converter progressively separates the lateral ground planes of the CPW until the propagating mode is confined exclusively on the central strip, thus becoming a PGL.

For designing a low-loss CPW-to-PGL mode converter, (1) its characteristic

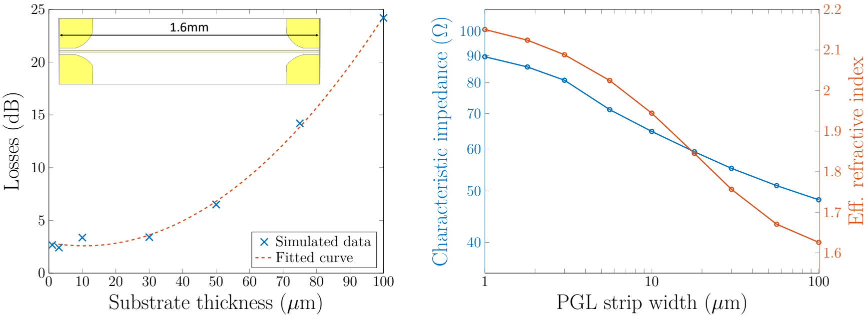

(a) **(b)**

Figure 3.6: Simulation results of PGL parameters. **(a)** Losses at 1 THz of a 1.6-mm-long PGL with CPW-PGL mode converters as a function of the silicon substrate thickness. **(b)** Characteristic impedance and effective refractive index of a PGL in 10-µm-thick silicon membrane substrate as a function of the PGL strip width.

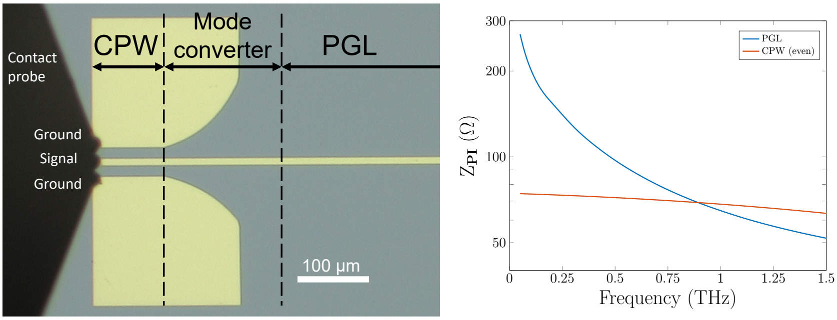

(a) **(b)**

Figure 3.7: The CPW-to-PGL mode converter can be used to excite a PGL with ground-signal-ground probes. **(a)** Micrograph of the ground-signal-ground probe contacting the CPW mode converter on the silicon-membrane substrate. **(b)** Power-current defined impedance, eq. (2.7), for PGL and CPW. The high-frequency dependence of the PGL's impedance will hinder a broadband impedance match with the less frequency-dependent CPW impedance.

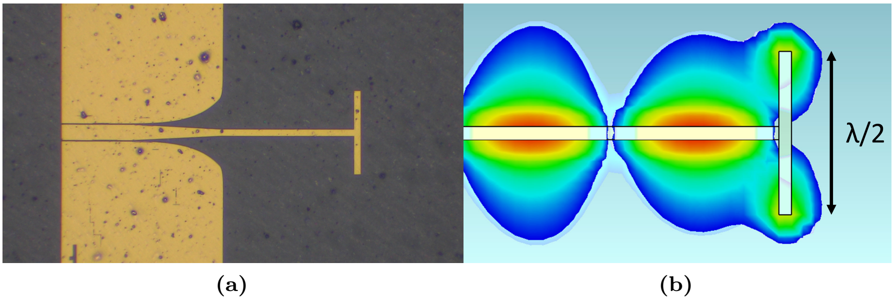

Figure 3.8: Layout of PGL Reflect standard. (a) Micrograph of one of the fabricated PGL Reflect standards on the PET substrate. **(b)** Electric-field distribution around the PGL Reflect standard, showing a minimum at the T-shaped junction: a short-circuit.

impedance was varied geometrically to minimise reflections, (2) small CPW strip and gap dimensions were avoided, which would increase conductor losses, and (3) the total length was chosen to minimise insertion losses, as a too-short converter would have high reflections, and a too-long converter would add unnecessary line losses. Unfortunately, the characteristic impedance of the PGL is very frequency-dependent, unlike the CPW's (Fig. 3.7b), and thus a broadband impedance match between the two is challenging.

3.3.3 Planar Goubau line calibration standards

To the best of the author's knowledge, no calibration standards for PGL had been reported before. Therefore, **Paper A** proposes multi-line TRL calibration standards, which enable setting the measurement reference plane in the PGL, effectively de-embedding the CPW-to-PGL mode transformers. Three Lines standards were designed with electrical lengths of $\lambda_g/4$, $3\lambda_g/4$ and $11\lambda_g/4$ at the geometrical centre frequency of the band, at 910 GHz. For the Reflect calibration standard, a highly-reflective element needs to be designed. Several designs of Reflect standards were tested using electromagnetic simulations. The best performance was achieved by a T-shaped structure terminating the planar Goubau line (Fig. 3.8.a) with a span of $\lambda_g/2$. The Reflect standard has a maximum electric field intensity at the ends of the T-sidearms (Fig. 3.8.b), creating a null of electric field intensity in the intersection; thus, the structure behaves as a short-circuit at the intersection point of the T-shaped structure. All fabricated devices were designed to have the same layout environment close to where the probes make contact, improving repeatability [110].

CHAPTER 4

Fabrication of PGL devices

This chapter briefly describes the fabrication technique of membrane-based PGL components. The PGLs with their corresponding dedicated calibration standards were fabricated in our in-house cleanroom using electron-beam lithography and evaporation of 20-nm-thick titanium and 350-nm-thick gold on top of the substrate. Throughout this thesis, chips were fabricated in two substrates: polyethene-terephthalate (PET) films, with a thickness of 23 µm, and high-resistivity silicon membranes with a thickness of 10 µm.

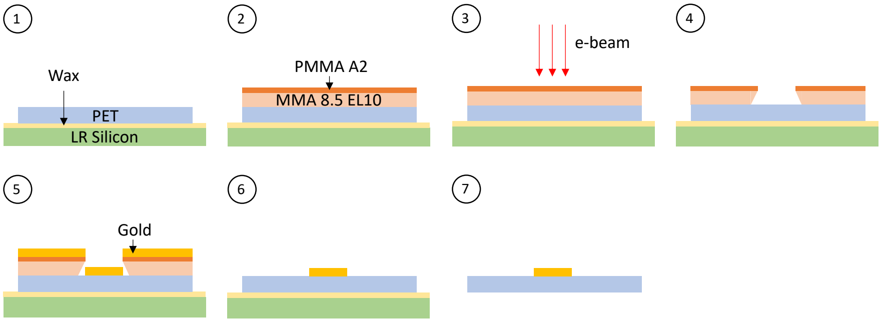

Figure 4.1: Sketch of the fabrication steps for the PET substrate. The figure is not to scale

The fabrication for the PET chip was done according to the process seen in

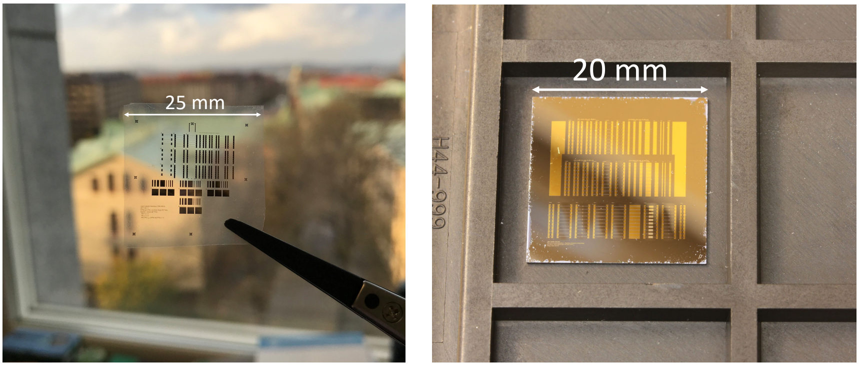

(a) **(b)**

Figure 4.2: Pictures of two chips fabricated on different substrates. **(a)** On polyethylene-terephthalate substrate and **(b)** on high-resistivity silicon membranes.

Fig. 4.1. First, the PET substrate was mounted onto a silicon wafer using wax (#1). The electron-beam lithography resist was added (#2), exposed (#3) and developed (#4). A 350-nm-thick layer of gold was deposited (#5), lift-off was done in acetone (#6), and finally, the plastic substrate was detached from the silicon carrier wafer (#7). Fig. 4.2a shows the finalised PET chip held against a background of a beautiful city.

The fabrication process for the high-resistivity silicon membranes was done with a 20 mm by 20 mm silicon-on-insulator wafer purchased from University Wafers. The top layer had 10-µm-thick high-resistivity (>10 kΩ cm float-zone) silicon, the oxide layer was 1 µm thick SiO_2, and the bulk silicon was 400-µm-thick. The fabrication steps are represented in Fig. 4.3. First, a silicon-on-insulator wafer is coated with a resist, exposed to electron-beam lithography (#1) and developed (#2). A 350-nm-thick gold layer was deposited (#3) and lift-off in acetone (#4). The silicon membranes were made by spinning a resist on the backside of the chip, exposing it to laser writer (#5), and developed to form the mask to etch the backside silicon (#6). The chip was mounted onto a carrier wafer and exposed to a Bosch process (#7). After etching, the carrier wafer was left in acetone for detachment (#8). Finally, the resist residues were removed with oxygen plasma (#9). Fig. 4.4 shows pictures of the 10-µm-thick silicon membranes.

A full description of both fabrication processes can be found in Appendix A.

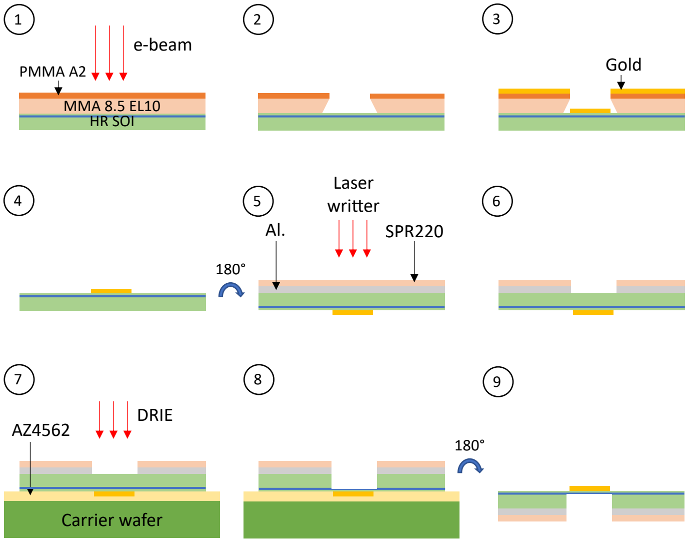

Figure 4.3: Sketch of the fabrication steps for the high-resistivity silicon membranes. The figure is not to scale

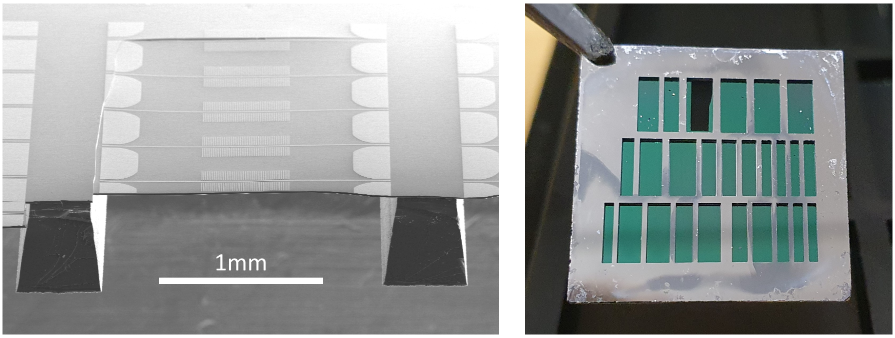

(a) **(b)**

Figure 4.4: Pictures of the silicon membranes (a) SEM profile picture of the silicon membranes, with the PGLs on top. Unfortunately, the silicon membrane cracked when the chip was cleaved to take the membrane picture. **(b)** Photograph of the backside of the chip shown in Fig. 4.2b, where the membranes have a dark-green colour. One of the top membranes was over-etched and later broke

CHAPTER 5

Terahertz characterisation of PGL components

This chapter starts by describing the experimental setup used for measuring the scattering parameters of the PGL components proposed in this thesis (Section 5.1). In following sections it presents the main measurements results of this thesis: the validation of the PGL calibration standards (Section 5.2), a loss comparison between PGL and CPW (Section 5.3), measurements of designed PGL devices (Section 5.4) and finally a demonstration of the PGL for spectroscopy of aqueous samples (Section 5.5).

5.1 Measurement setup

The devices were characterised by measuring 2-port S-parameters. Fig. 5.1a shows a sketch of the measurement setup including:

- **Vector Network analyser (VNA):** model Keysight N5242B (10 MHz to 26.5 GHz). The intermediate-frequency bandwidth was set to 50 Hz for lowering the noise floor.

- **Frequency extenders:** when measuring S-parameters at THz frequencies, signal multipliers are used to convert the VNA's signal into a higher frequency signal, covering the band which needs to be measured. Frequency extenders were used, VDI WR1.5SAX and VDI WR1.0SAX, for frequency bands WR1.5(0.5 THz to 0.75 THz) and WR1.0 (0.75 THz to

1.1 THz), respectively. For the WR1.5SAX extenders the typical dynamic range is around 90 dB and for the WR1.0SAX is around 70 dB.

- **Ground-signal-ground probes (Fig. 5.1b)**: used as the interface between the frequency extenders and the measured devices. The probes couple the fields to the devices under test from the rectangular waveguides of the frequency extenders. Two pairs of cascade's T-Wave probes [108] were used for measuring between 0.5 THz and 1.1 THz (for WR 1.5 and WR1.0 bands) and have a probe pitch of 25 µm.

A picture of the entire measurement setup can be seen in Fig. 5.1c.

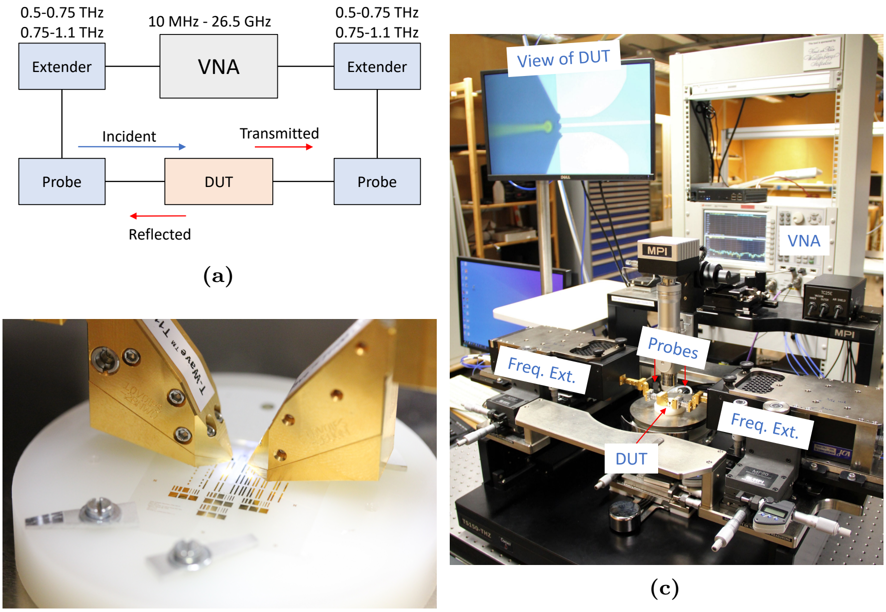

(a)

(b)

(c)

Figure 5.1: (a) Sketch of on-wafer S-parameter measurements setup measuring a generic Device Under Test. **(b)** Picture of probes while measuring devices in the PET chip on top of the supporting substrate. **(c)** Picture of the setup used to measure the S-parameters of the devices presented in this thesis. The setup consists of a VNA with frequency extenders and the probes shown in (b).

The fabricated chips were placed on a supporting substrate, isolating the devices from the metal chuck. The use of a supporting substrate is critical in the case of the PET substrate, which is just 23 µm thick, whereas the silicon membrane is suspended on top of the 400-µm-thick silicon chip. Since the PGL's field distribution decays exponentially in the transverse direction, its propensity to leak power is affected by other surrounding materials, such as the supporting substrate. For that reason, the supporting substrate was selected with a lower refractive index than the substrates to avoid leakage from the PGL's propagating mode [87]. The supporting substrate was chosen as a 6 cm in diameter and 1-cm-thick polyethylene (PE) cylinder, with a relative permittivity of $\epsilon' = 2.3\epsilon_0$ and a loss tangent of $\tan(\delta) = 0.004$. The chip was clamped onto the supporting substrate to avoid movement during measurements. The supporting substrate has a 1-mm-deep and 1-mm-wide cavity, which is aligned with the measured devices in the PET chip to create an air-suspended membrane (see Fig. 5.9a) and avoid radiation losses. The devices on the silicon membrane are suspended in air (Fig. 4.4a) and therefore do not need a cavity in the substrate to create a suspended membrane.

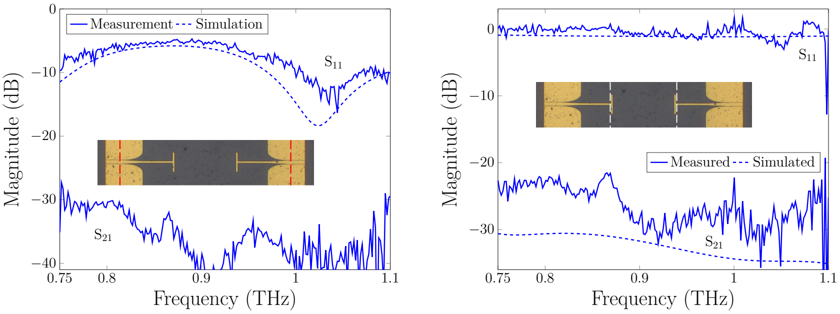

(a) **(b)**

Figure 5.2: Simulations and measurements of the PGL Reflect have good agreement when using (a) a established CPW calibration as well as with (b) the proposed PGL calibration. S-parameter comparison of simulations (dashed line) and measurements (solid line) of the Reflect standard. In (a) the simulated S_{21} is lower than −40 dB in all the band. The inset shows a micrograph of the PGL Reflect fabricated in the PET substrate, showing the calibration plane of the simulation and measurements depicted as a dashed line.

5.2 PGL calibration standards

The Through and Line standards for a PGL TRL calibration have a trivial design and a known frequency response. On the other hand, the designed Reflect standard presented in **Paper A** and Section 3.3.3 needs to be characterised, first with a well-established CPW calibration and then with the proposed PGL calibration. Fig.5.2a shows good agreement between simulations and measurements of the designed and fabricated Reflect standard on PET substrate. These measurements were calibrated with CPW multi-line TRL standards that set the reference plane 105 µm inside the CPW, marked with a discontinuous red line in the inset of the figure. Simulated S_{21} is lower than -95 dB in all the band, whereas the measured S_{21} lies at the noise-floor level, around -35 dB.

The Reflect was measured again, this time after calibrating with the multi-line TRL calibration standards for PGL proposed in **Paper A**, which set the calibration plane after the CPW-to-PGL mode converter (see dashed line in the inset of Fig. 5.2b). The measurements were done using a different Reflect standard from the one used for calibrating. The S-parameter measurement results of the PGL Reflect show to have high and wideband reflection characteristics, with over -1.1 dB in all the band (Fig. 5.2b). The transmission measurements are very low, below -21 dB, as expected. Simulations using a PGL wave-port agreed with the measurements results, having high reflectivity and low transmission. The simulation results showed in Fig. 5.2b were obtained by exciting a PGL line terminated in the Reflect standard and de-embedding the PGL line in the simulation software.

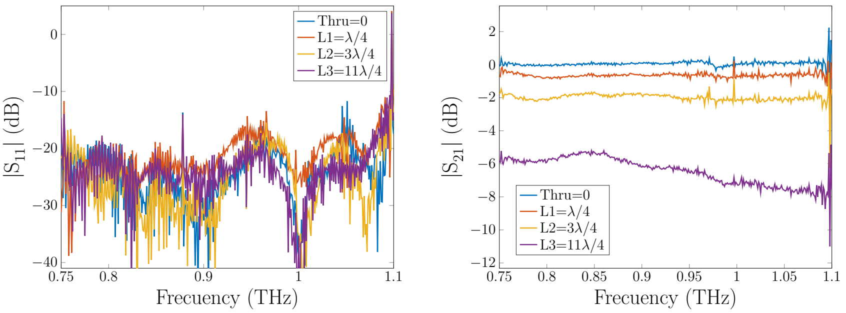

(a) **(b)**

Figure 5.3: Measurements of PGLs of different lengths after calibrating demonstrate a correct de-embedding of the CPW-PGL transitions. Measured magnitude of **(a)** reflection (S_{11}) and **(b)** transmission (S_{21}) of the Through and multiple lines in the calibration standard. The low value of $|S_{11}|$ indicates a correct de-embedding of the CPW-PGL mode transformer, while the values of $|S_{21}|$ yield expected behaviour for lines at these frequencies.

In addition to the PGL Reflect, the PGL Through and Line standards were measured after PGL calibration, choosing structures that weren't used during the calibration. Fig. 5.3 shows the measured transmission and reflection of Through and Lines from the calibration standards after applying the

PGL calibration. The low levels of $|S_{11}|$ and the smooth $|S_{21}|$ indicate that the calibration method has correctly de-embedded the CPW-to-PGL mode converter.

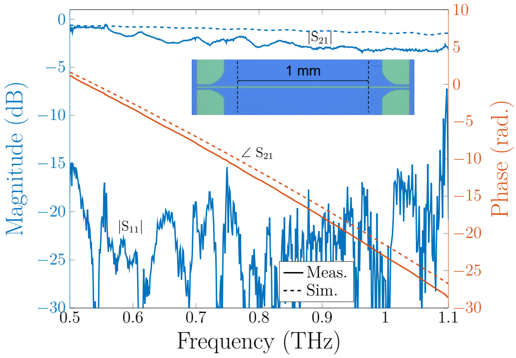

Figure 5.4: Simulations and measurements of a 1-mm-long PGL on silicon membrane after calibrating with the proposed PGL TRL standards. S-parameter comparison of simulations (dashed line) and measurements (solid line). Simulated S_{11} results are below $-39\,\mathrm{dB}$ in all the band, whereas measured S_{11} are limited by the noise floor, around $-20\,\mathrm{dB}$. Inset shows a micrograph of the 1-mm-long PGL, with the calibration plane of the simulation and measurements depicted as a dashed line, set after the CPW-to-PGL mode converter, along the PGL.

Fig. 5.4 shows the simulated and measured S-parameters for a 1-mm-long PGL on the silicon-membrane substrate using the PGL TRL calibration. The results of the magnitude of the transmission, $|S_{21}|$, show to be flat except for a subtle decrease proportional to the frequency for both measurements and simulations. The phase results have a linear frequency response, indicating negligible PGL dispersion. There is a slight difference in the slope of the phase of the transmission between measurements and simulations, indicating that the substrate might be thicker or have a higher permittivity value than the one used for simulations, based on literature values [105]. The measured reflection parameter, S_{11}, shows to be typically below $-20\,\mathrm{dB}$—the noise floor of reflection measurements—with higher values at the sides of the rectangular waveguide bands. Ideally, these values should be as low as possible. Still, the reflection coefficient is very susceptible to the probing conditions, especially when having the probing area behind the reference plane, making reflection measurements more unreliable than transmission measurements. Overall, the developed PGL calibration standards set the calibration plane along the PGL, accurately de-embedding the CPW-to-PGL mode converter and probe-chip interface.

5.3 Planar waveguide loss

At THz frequencies, the available power of electronic sources is lower than at lower frequencies, and conductor and radiation losses increase with frequency. Thus it is essential to minimise losses to have a higher dynamic range and SNR.

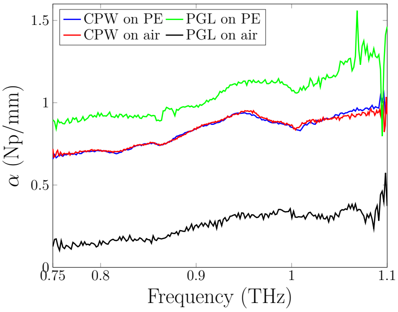

Figure 5.5: The PGL losses drop dramatically when an electrically-thin substrate is used. The figure shows the attenuation coefficient measurements of a 1 mm long CPW and PGL in PET substrate. Measurements were done on two setups: placing the device on top of a polyethylene (PE) supporting substrate or suspending it on air, creating a membrane (see Fig. 5.9a).

Paper B compares the measured attenuation constants of two planar metal waveguides, a CPW and a PGL, fabricated in the same ultra-thin PET film chip. For each waveguide, CPW or PGL, the measurements were calibrated using dedicated calibration standards included in the same chip, and a 1-mm-long line was measured for each case. Fig. 5.5 shows the measured CPW and PGL attenuation constant for two cases: having the line on top of the cavity in the supporting substrate, creating a membrane, and having the line directly on top of the supporting substrate. When using the PE supporting substrate, the CPW has lower losses than the PGL. However, when the measured waveguides are suspended on air—by placing them on top of a micromachined hole in the PE supporting substrate—the losses of the PGL drop drastically, whereas the CPW losses remain unchanged. When suspended in air, the PGL becomes a more power-efficient planar waveguide compared to the CPW, with an attenuation coefficient of 0.32 Np/mm at 1 THz. The main reason for this is that the PGL's field distribution is much broader, making its phase velocity higher than in the supporting substrate's. In contrast, the CPW has a more confined field, and the phase velocity is more affected by the PET substrate, producing a lower phase velocity than the supporting substrate's.

5.4 Planar Goubau line components

Some PGL design components have been suggested, but many of them lack a clear design procedure. In this thesis, I proposed three PGL circuit components measured at THz frequencies and with a straightforward design procedure: a stop-band filter (**Paper C**), an impedance-matched load (**Paper D**), and a power-divider (**Paper E**).

The PGL stopband filter presented in **Paper C** is based on a PGL which is periodically loaded with capacitively-coupled $\lambda/2$ resonators (Fig 5.6a). The electrical behaviour of the filter is modelled using a transmission-line model of a repeating unit cell consisting of a shunt resonator coupled to the line by a capacitance (Fig. 5.6b). Fig. 5.6c shows the measured magnitude of S_{21} compared with electromagnetic simulations and the proposed transmission-line model showing good agreement between them.

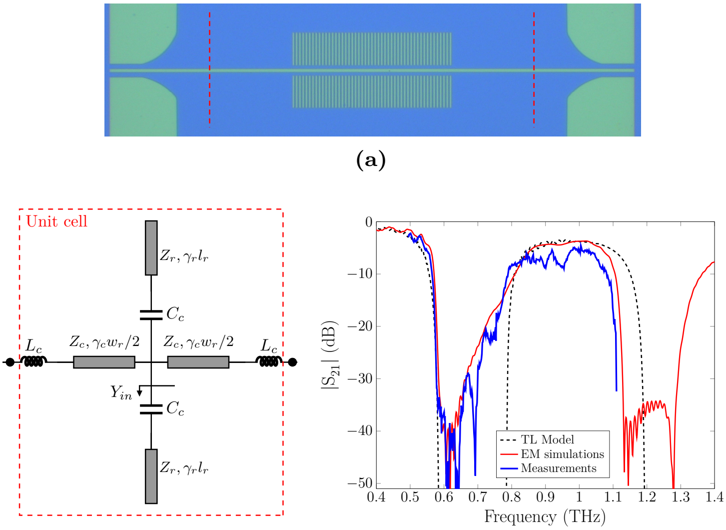

(a)

(b)

(c)

Figure 5.6: Proposed PGL filter based on coupled resonators. (a) Micrograph of the PGL filter with CPW-PGL transitions fabricated in the silicon membrane. The red lines show the reference plane of S-parameter results. **(b)** Transmission-line model of the filter's unit cell. **(c)** Magnitude of S_{21} of the filter, comparing measurements with simulations and the transmission line model, showing good agreement.

The impedance-matched load presented in **Paper D** is based on an exponentially-tapered corrugated PGL (Fig. 5.7a). As seen in Section 2.6.1, longer corrugations increase the effective refractive index of the TM mode, its confinement to the metal and its conductor loss, but corrugations longer than $\lambda/4$ cannot propagate TM modes. The corrugations are exponentially increased over distance, avoiding reflections and increasing losses progressively. The ohmic losses drastically increase when the corrugations are nearly $\lambda_c/4$-long for a given frequency. Fig. 5.7b shows the measured magnitude of S_{11} compared to electromagnetic simulations of the proposed load, being the measurements limited by the noise-floor of the measurements setup, around -20 dB. Simulations of the same load made using a perfect electric conductor show a high magnitude of S_{11}, meaning that the matched load works due to ohmic losses and not radiation.

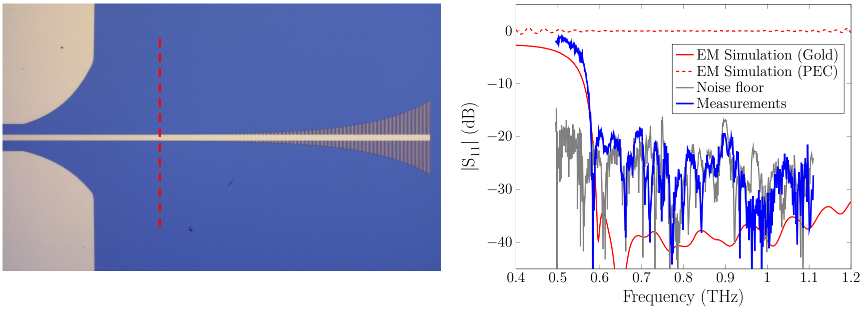

(a) **(b)**

Figure 5.7: Proposed PGL impedance-matched load based on an exponentially-tapered corrugated line. (a) Micrograph of the PGL matched load fabricated on a silicon membrane. The red line shows the reference plane of S-parameters. **(b)** Magnitude of S_{11} of the filter, comparing measurements with simulations, showing good agreement. The simulation with a perfect electric conductor (PEC) load shows that conductors and not radiation produce losses.

The PGL power divider presented in **Paper E** is based on the combination of two concepts already mentioned in this thesis: the short-circuit proposed in **Paper A** and the coupled lines used for the filter proposed in **Paper C**. The output lines are coupled to the standing wave of the input line caused by a PGL short-circuit (Fig. 5.8a). This design achieves higher output power, lower input reflections and higher isolation between output ports than T- or Y-shaped line junctions, as shown in **Paper E**. Fig 5.8b-c show measurement results of the power divider, together with electromagnetic simulations. If the power split and line losses are discounted, the power divider has an approximate insertion loss of around 0.5 dB around its centre frequency.

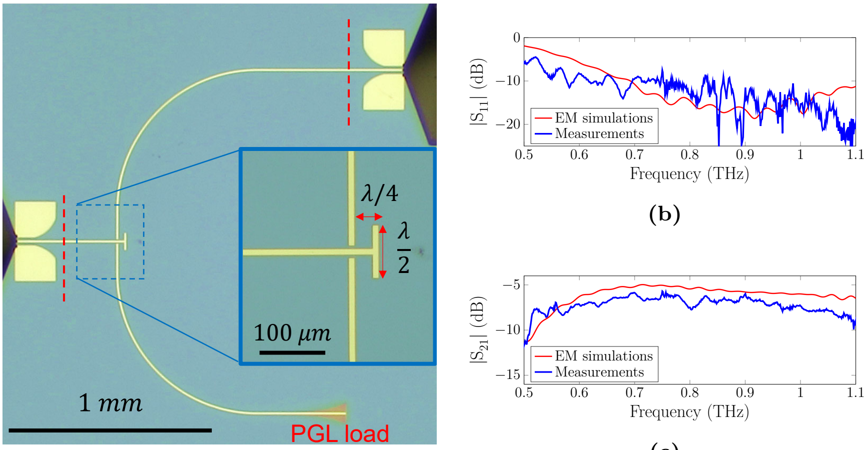

(a) **(b)** **(c)**

Figure 5.8: Proposed PGL power divider based on output lines coupled to the input port standing wave. **(a)** Micrograph of the PGL power divider on silicon membrane, designed at a centre frequency of 0.9 THz, being measured with probes. Red dashed lines indicate the measurements reference plane. One of the output ports of the power divider was terminated with a PGL impedance-matched load, as required for two-port S-parameter measurements. **(b)** Magnitude of S_{11}, showing relatively low input port reflections. **(b)** Magnitude of S_{21}, where frequencies away from the design frequency show lower transmission levels.

5.5 Spectroscopy of aqueous samples

One of the characteristics of the PGL is its large field extension compared to other planar transmission lines. This makes the PGL an attractive candidate to be combined with microfluidic channels to create liquid sensing platforms at THz frequencies. When creating a spectroscopy setup for aqueous samples, the goal is to detect small changes in the real and imaginary parts of the sample's refractive index. Unfortunately, liquid water has an extremely high dielectric attenuation constant around THz frequencies, in the order of 100 dB/mm [111], which can reduce the SNR and thus the sensitivity of the system. Therefore, it is essential to have control of the sample's dimensions and avoid unnecessary losses. Microfluidic channels offer an excellent solution for the control of the dimensions of the sample with micrometre precision, avoiding its evaporation and guiding liquid samples into the sensing area of a chip. The microfluidic channels used in this thesis were fabricated in polydimethylsiloxane (PDMS) with a rectangular cross-section channel of width $l_s = 120\,\mu\text{m}$ and height 95 µm (see Fig. 5.9a). The microfluidic channel was aligned under the microscope and attached to the PGL using a metal clamp that tightened the PDMS to the supporting substrate (Fig. 5.9b). Clamping the microfluidic channel allowed the possibility to change channels without the need to fabricate new structures. The sample under test was delivered to the microfluidic channel using a manually-operated syringe through tubings connected to the PDMS microfluidic channel.

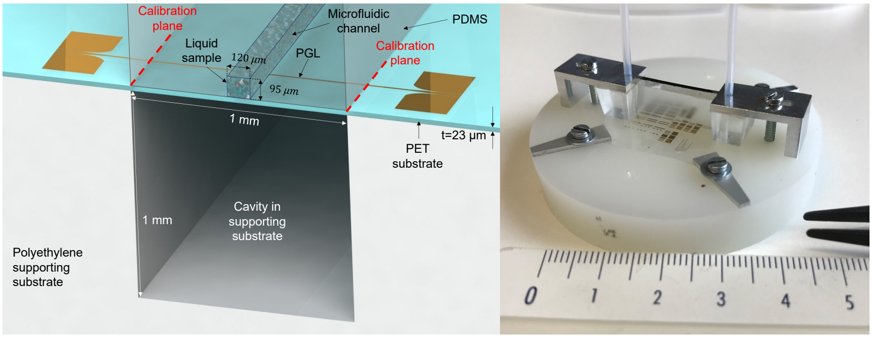

(a) **(b)**

Figure 5.9: **(a)** Representation of the PGL crossing the microfluidic channel containing the aqueous samples. Probes contact the CPW-to-PGL transitions at the edge of its sides. **(b)** Photograph showing the PET chip with devices held on to the PE supporting substrate. The PDMS with the microfluidic channels is clamped to the supporting substrate and remains in contact with the devices. Tubes are attached to the microfluidic channel to pump the samples.

The sample's refractive index was obtained from the measured complex transmission parameter, S_{21}, of a PGL crossing the microfluidic channel containing the sample, similarly to **Paper C**, in which a CPW was used instead. The diagram in Fig. 5.10 offers an overview of the process to obtain the sample's refractive index from the transmission measurements, consisting of two main steps: (1) obtaining the effective refractive index (or propagation constant) of the PGL section with the sample, and (2) translating this effective refractive index into the sample's refractive index.

Considering a reference sample with a known refractive index, $\tilde{n}_r$, the effective refractive index of the PGL with the sample, $\tilde{n}_e$, can be calculated using relative measurements as:

$$\tilde{n}_e = \tilde{n}_r - \frac{\ln\left[S_{21}^{(s)}/S_{21}^{(r)}\right]}{jk_0 l_s}, \tag{5.1}$$

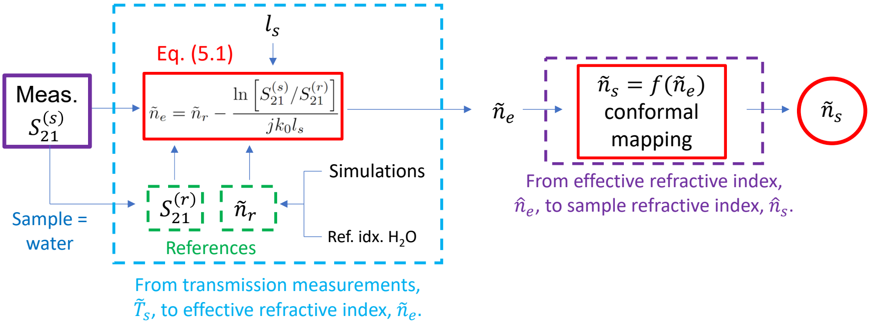

Figure 5.10: Diagram showing how the sample's complex refractive index, $\tilde{n}_s$ was obtained from the transmission measurements $S_{21}^{(s)}$.

where $S_{21}^{(s)}$ and $S_{21}^{(r)}$ are the complex transmission coefficient for sample and reference, respectively, k_0 is the vacuum wavenumber, and l_s is the effective length of the sample. The reference effective refractive index, $\tilde{n}_r$, for the PGL was obtained using electromagnetic simulation results of a PGL with water [112]. Water is a sample that has been measured extensively at THz frequencies and thus has accurate material properties. After calculating the effective refractive index of the PGL containing the sample, with the eq. (5.1), the sample's permittivity was calculated using conformal mapping based on electromagnetic simulations of the setup, sweeping the sample's real and imaginary refractive index.

Fig. 5.11 shows the calculated sample's real and imaginary refractive index for water/propan-2-ol mixtures—between 50 and 100%, in steps of 10%—using pure deionised water as a reference sample. Each sample was measured five times in consecutive VNA frequency sweeps, and their mean and standard deviation were calculated. Both the magnitude and phase measurements show sufficient SNR for distinguishing between samples despite the high losses of the aqueous samples, being magnitude measurements more sensitive to changes than phase measurements. The sensitivity of the setup can be defined as the slightest possible refractive index change that can be detected from 5 measurements with a probability of 95%. With that definition, the sensitivity of the setup is $\Delta n = 0.03$ for the real part of the refractive index and $\Delta\kappa = 0.0035$ for the imaginary part. This sensitivity is similar to the CPW system presented in **Paper F**. These results show better performance than on-chip systems measuring aqueous samples with time-domain spectroscopy, the most popular experimental setup for measuring the complex transmission of THz waves. Time-domain spectroscopy could not resolve measurements of water above

0.5 THz using a similar PGL setup [36], or needed to avoid direct contact between the line and sample, sacrificing sensitivity, to achieve sufficient SNR [113].

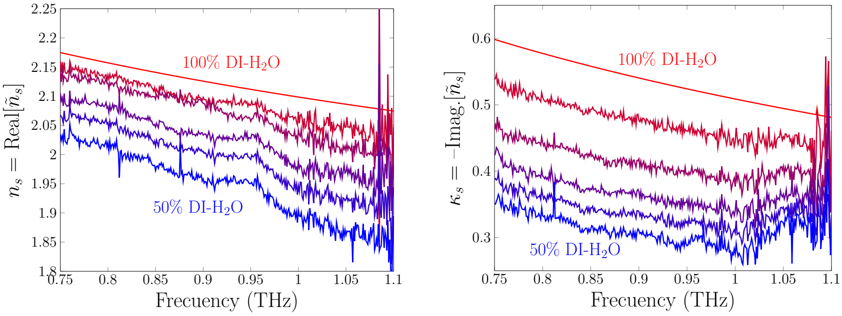

(a) **(b)**

Figure 5.11: The sample gradient yields distinguishable magnitude and phase changes in the transmission. Extracted **(a)** real and **(b)** imaginary part of the sample's refractive index, calculated using the process shown in Fig. 5.10. Samples consist of propan-2-ol/deionised-water mixtures with water volume concentration from 50% to 100% in steps of 10%. Measurements were performed five times in consecutive frequency sweeps.

It is worth noting that the PDMS channel swells by pure propan-2-ol, which reduces the microfluidic width to 113 µm. However, samples with a propan-2-ol concentration lower than 50% showed no impact on the channel width, and only samples between 0% and 50% propan-2-ol concentration were measured. Similarly, propan-1-ol (with a similar Hildebrand solubility parameter and dipolar moment as propan-2-ol) was reported to have a swelling factor of 9% in PDMS, whereas water produced no swelling [114].

CHAPTER 6

Concluding remarks and future outlook

This thesis has presented the study of planar Goubau lines (PGL) at THz frequencies, developed calibration standards and circuit elements, and performed spectroscopy measurements of high-loss aqueous samples.

Paper A presents the first calibration standards proposed for PGL. The PGL calibration standards, based on multi-line Through-Reflect-Line, enable de-embed the mode converters used to excite the PGL and set the calibration plane along the PGL. The Reflect standard is designed as a $\lambda/2$ T-shaped structure and forces the electric field to zero at its junction, behaving like a short circuit. The calibration standards are demonstrated by measuring PGLs of different lengths, where the low levels of $|S_{11}|$, S_{21} flat magnitude and adequate phase delay show that the mode converters have been de-embedded correctly.

At terahertz frequencies, ohmic and radiation losses are high and must be minimised to avoid lowering the SNR. **Paper B** presents how PGLs fabricated on electrically-thin substrates drastically reduce their radiation loss, becoming more power-efficient than a coplanar waveguide in the same substrate.

Designing components for PGL is challenging for the lack of ground plane and the weak relation between metal strip width and impedance. **Papers C, D and E** present PGL circuit components designed and measured at THz frequencies, between 0.5 and 1.1 THz. **Paper C** presents a stopband filter based on capacitively-coupled open-ended $\lambda/2$ resonators periodically placed along the PGL. The filter's functioning is explained using a transmission line model of the periodic unit cell, showing good agreement with measurements and simulations. This component is an alternative stopband filter design that is easy to tune and has relatively low insertion loss. **Paper D** presents a PGL impedance-matched load based on an exponentially-tapered and densely-corrugated PGL. This design with dense corrugations avoids using a supplementary lower-conductivity material to achieve high conductor loss, simplifying the fabrication process. The corrugations steeply increase the conductor loss, the phase constant and the confinement of the field when the corrugation length approaches $\lambda/4$. The smooth corrugation taper ensures an impedance match to avoid reflections. **Paper E** presents a PGL power divider based on capacitively-coupled lines to the standing wave produced by a short circuit in the input port. The proposed design has higher output power, lower reflections and better isolation between output ports than a Y-shaped junction.

Finally, this thesis presents the use of PGLs with microfluidic channels to measure changes in the real and imaginary refractive index of water/isopropan-2-ol mixture samples, similarly to **Paper F**, where CPWs were used instead. These on-chip measurements can detect slight sample differences up to 1 THz, whereas previous on-chip measurements using time-domain THz spectroscopy either lacked the SNR or sensitivity.

In summary, this thesis presents evidence to support that PGL holds promise as a power-efficient metal planar waveguide for THz applications, with an attenuation constant around 3 dB/mm at 1 THz for electrically-thin suspended substrates. Suspended silicon membranes have shown to be a suitable substrate of choice for their ability to be made ultra-thin using a relatively easy fabrication process and having plenty of mechanical strength. The relatively low losses, the contribution of circuit elements with a straightforward design, and calibration standards increase the PGL's possibilities as a planar waveguide to use at THz frequencies.

Other waveguides exist with a higher power efficiency at THz frequencies than PGLs, for example, planar dielectric waveguides and hollow rectangular waveguides. However, the PGL could offer the niche of being planar, easy to fabricate and capable of using circuit components. This thesis may also inspire component designs for the Sommerfeld wire and the Goubau line, which have even higher power efficiency than rectangular waveguides.

CHAPTER 7

Summary of appended papers

Paper A

Multiline TRL Calibration Standards for S-parameter Measurement of Planar Goubau Lines from 0.75 THz to 1.1 THz

This work presents a calibration standard for planar Goubau lines based on Through-Reflect-Line (TRL) standards. The calibration standards are validated with an established CPW calibration and with the proposed PGL calibration, showing good agreement with simulations in both cases. The calibration is used to demonstrate measurements of a 1 mm long PGL between 0.75 THz to 1.1 THz, with losses between 0.13 Np/mm to 0.35 Np/mm, negligible dispersion and wide-band characteristics. The proposed calibration standard opens up possibilities for studying and measuring the PGL and its circuit elements in detail.

My contributions: design, measurements, post-processing, interpretation, writing.

Paper B

Transmission Loss in Coplanar Waveguide and Planar Goubau Line between 0.75 THz and 1.1 THz

This work compares the losses of 1 mm CPW and PGL under two circumstances: with the polyethene supporting substrate below the device and with the device being suspended on air. The CPW has a lower attenuation constant than the PGL if the supporting substrate is present below the devices. When the supporting substrate is removed from below the measured device, maintaining the substrate suspended on air, the attenuation constant of the CPW remains unaltered, whereas the PGL's drops drastically, becoming more power-efficient than the CPW.
My contributions: design, measurements, post-processing, writing.

Paper C

Capacitively-coupled resonators for terahertz planar-Goubau-line filters

This work presents a bandstop filter design for PGL based on capacitively-coupled $\lambda/2$ resonant lines, showing relatively low insertion losses, high stop-band rejection, and a simple design. It demonstrates the design by measuring a filter with 49 pairs of resonators between 0.5 and 1.1 THz using VNA and ground-signal-ground probes, showing good agreement between measurements and simulations. Future work could study modulating the electrical length of the resonators to produce a desired stopband.
My contributions: design, measurements, post-processing, interpretation, writing.

Paper D

A corrugated planar-Goubau-line matched load for terahertz waves

This work presents an impedance-matched load for PGL with low reflections based on an exponentially-tapered corrugated PGL. The corrugations increase the ohmic losses of the PGL by inducing surface currents in its contour from the magnetic field. The matched load was designed to have high corrugation density to maximise the ohmic losses induced in the corrugations, thus avoiding

using a second lower-conductivity material, simplifying the fabrication process. The matched load was measured between 0.5 and 1.1 THz using VNA and ground-signal-ground probes, showing good agreement between measurements and simulations. The return losses were better than 19 dB in the bandwidth of operation, being limited by the noise floor of the reflection measurements.
My contributions: design, measurements, post-processing, interpretation, writing.

Paper E

A capacitively-coupled terahertz planar-Goubau-line power divider

This work presents an equal-split power divider design for PGL based on lines coupled to the standing wave produced by a short circuit. Results show higher delivered power to the output ports than simpler T- or Y-power divider designs, lower input port reflection, and higher isolation between ports. The disadvantage is the lower bandwidth of operation, showing poor performance at lower frequencies. The power divider was demonstrated by being measured with VNA between 0.5 and 1.1 THz, showing good agreement with simulations, and an insertion loss lower than 1 dB for the bandwidth of operation if reflection, power-split and line losses are discounted.
My contributions: design, measurements, post-processing, interpretation, writing.

Paper F

On-Chip Characterisation of High-Loss Liquids between 750 GHz and 1100 GHz

The characterisation of aqueous samples is relevant since it is the native environment of biological samples, and their extreme absorption poses a big challenge to chip measurements. This work performed THz transmission spectroscopy of high-loss aqueous samples using a chip excited with VNA and probes. The chip integrated CPWs and microfluidic channels, which would guide and control sample volumes. Similar attempts using THz time-domain spectroscopy in chips could not resolve water measurements above 0.5 THz or had to avoid having the sample on the transmission line's region with the strongest field intensity, losing sensitivity. The proposed solution yielded high-SNR measurements and took a step towards a miniaturised system for

THz spectroscopy of high-loss liquids.
My contributions: design, measurements, post-processing, interpretation, writing.

APPENDIX A

Fabrication steps

The fabrication for the polyethylene-terephthalate substrate was done according to the following steps, represented in Fig. 4.1:

1. Mount the 23-µm-thick PET film on low-resistivity 2-inch silicon wafers using thin-film wax.
2. Spin electron-beam lithography resist and auxiliary layers:
   a) Spin HMDS (negligible thickness) at 3000 rpm for 30 s. Acceleration time: 1 s. No baking.
   b) Spin MMA 8.5 EL10 (450 nm thick) at 3000 rpm for 30 s. Acceleration time: 1 s. Bake in oven for 10 min at 110 °C. Spin PMMA A2 (70 nm thick) at 3000 rpm for 30 s. Acceleration time: 1 s. Bake in oven for 10 min at 110 °C.
   c) Spin Espacer 300Z (20 nm thick) at 1500 rpm for 60 s. Acceleration time: 1 s. Bake on hot plate for 90 s at 80 °C.
3. e-beam lithography (current 30 nA, dose 320 µC/cm^2).
4. Substrate development:
   a) Developed in IPA:DI-H_2O in 10:1 volume ratio for 40 seconds.
   b) Ash O_2 plasma for 5 s at 40 W.
5. Deposit Ti/Au 20/350 nm.

6. Lift-off in 65 °C acetone.

7. Detach the PET film from the silicon wafer

The fabrication steps for the PGLs on high-resistivity silicon membranes are the following, and are represented in Fig. 4.1:

1. Spin of the electron-beam lithography resist and auxiliary layers in a silicon-on-insulator (SOI) wafer with 10-µm high-resistivity silicon layer, and 1-µm silicon oxide layer: HMDS process 100 °C 60 seconds. Spin MMA 8.5 EL10 (450 nm thick) at 3000 rpm for 30 s. Acceleration time: 1 s. Bake at 110 °C for 10 min. Spin PMMA A2 (70 nm thick) at 3000 rpm for 30 s. Acceleration time: 1 s. Bake at 110 °C for 10 min. e-beam lithography (current 120 nA, initial dose 320 µC/cm^2).

2. Substrate development: Developed in IPA:DI-H_2O in 10:1 volume ratio for 40 seconds. Ash O_2 plasma at 40 W for 5 s.

3. Deposited Ti/Au 10/350 nm.

4. Lift-off in 65 °C acetone and 65 °C IPA.

5. Turn chip face down. Sputtering 20 nm of aluminum on backside of silicon on insulator chip. HMDS process at 100 °C for 60 seconds. Spin SPR220-3.0 at 3000 rpm for 30 s. Acceleration time: 0.3 s. Bake on hot-plate for 90 s at 115 °C. Laser writer exposure.

6. Develop resist and continue etching aluminum in MF24A.

7. Spin resist AZ4562 on 6-inch carrier wafer at 3000 rpm for 30 s. Acceleration time: 0.3 s. No baking. Place SOI chip face down and gently press it into the carrier wafer. Bake at 120 °C for 90 min. Deep reactive-ion etching (Bosch process). Gases: $SF_6 + O_2$. Passivation: C_2F_8. Etching rate: 1 µm per cycle.

8. After etching, leave 48 hours in room temperature acetone to detach chip from carrier wafer by dissolving the resist AZ4562.

9. Remove resist residues with O_2 plasma.

References

[1] T. Phillips and J. Keene, "Submillimeter astronomy (heterodyne spectroscopy)," *Proceedings of the IEEE*, vol. 80, no. 11, pp. 1662–1678, 1992. DOI: `10.1109/5.175248`.

[2] H. J. Song and T. Nagatsuma, "Present and future of terahertz communications," *IEEE Transactions on Terahertz Science and Technology*, vol. 1, no. 1, pp. 256–263, 2011. DOI: `10.1109/TTHZ.2011.2159552`.

[3] P. Bawuah and J. A. Zeitler, "Advances in terahertz time-domain spectroscopy of pharmaceutical solids: A review," *TrAC - Trends in Analytical Chemistry*, vol. 139, p. 116 272, 2021. DOI: `10.1016/j.trac.2021.116272`.

[4] R. Appleby and H. B. Wallace, "Standoff detection of weapons and contraband in the 100 GHz to 1 THz region," *IEEE Transactions on Antennas and Propagation*, vol. 55, no. 11 I, pp. 2944–2956, 2007. DOI: `10.1109/TAP.2007.908543`.

[5] E. Pickwell and V. P. Wallace, "Biomedical applications of terahertz technology," *Journal of Physics D: Applied Physics*, vol. 39, no. 17, pp. 301–310, 2006. DOI: `10.1088/0022-3727/39/17/R01`.

[6] G. Acbas, K. A. Niessen, E. H. Snell, and A. G. Markelz, "Optical measurements of long-range protein vibrations," *Nature Communications*, vol. 5, pp. 1–7, 2014. DOI: `10.1038/ncomms4076`.

[7] L. Rayleigh, " XVIII. On the passage of electric waves through tubes, or the vibrations of dielectric cylinders," *The London, Edinburgh, and Dublin Philosophical Magazine and Journal of Science*, vol. 43, no. 261, pp. 125–132, 1897. DOI: `10.1080/14786449708620969`.

[8] T. Yoneyama, S. Fujita, and S. Nishida, "Insulated Nonradiative Dielectric Waveguide for Millimeter-Wave Integrated Circuits," *IEEE Transactions on Microwave Theory and Techniques*, vol. 31, no. 12, pp. 1002–1008, 1983. DOI: `10.1109/TMTT.1983.1131652`.

[9] T. Itoh, "Overview of Quasi-Planar Transmission Lines," *IEEE Transactions on Microwave Theory and Techniques*, vol. 37, no. 2, pp. 275–280, 1989. DOI: `10.1109/22.20052`.

[10] D. D. Grieg and H. F. Engelmann, "Microstrip—A New Transmission Technique for the Kilomegacycle Range," *Proceedings of the IRE*, vol. 40, no. 12, pp. 1644–1650, 1952. DOI: `10.1109/JRPROC.1952.274144`.

[11] C. P. Wen, "Coplanar Waveguide: A Surface Strip Transmission Line Suitable for Nonreciprocal Gyromagnetic Device Applications," *IEEE Transactions on Microwave Theory and Techniques*, vol. 17, no. 12, pp. 1087–1090, 1969. DOI: `10.1109/TMTT.1969.1127105`.

[12] J. B. Knorr and K. D. Kuchler, "Analysis of Coupled Slots and Coplanar Strips on Dielectric Substrate," *IEEE Transactions on Microwave Theory and Techniques*, vol. 23, no. 7, pp. 541–548, 1975. DOI: `10.1109/TMTT.1975.1128624`.

[13] T. Akalin, A. Treizebré, and B. Bocquet, "Single-wire transmission lines at terahertz frequencies," *IEEE Transactions on Microwave Theory and Techniques*, vol. 54, no. 6, pp. 2762–2767, 2006. DOI: `10.1109/TMTT.2006.874890`.

[14] T. Schaich, D. Molnar, A. Al Rawi, and M. Payne, "Analytic modelling of a planar Goubau line with circular conductor," *Scientific Reports*, vol. 10, no. 1, pp. 1–10, 2020. DOI: `10.1038/s41598-020-77703-w`.

[15] H. Barlow and A. Cullen, "Surface waves," *Proceedings of the IEE - Part III: Radio and Communication Engineering*, vol. 100, no. 68, pp. 329–341, 1953. DOI: `10.1049/pi-3.1953.0068`.

[16] K. Uller, "Beiträge zur Theorie der Elektromagnetischen Strahlung," Ph.D. dissertation, University of Rostock, 1903, p. 82.

[17] J. Zenneck, "Über die Fortpflanzung ebener elektromagnetischer Wellen längs einer ebenen Leiterfläche und ihre Beziehung zur drahtlosen Telegraphie," *Annalen der Physik*, vol. 328, no. 10, pp. 846–866, 1907. DOI: `10.1002/andp.19073281003`.

[18] A. Sommerfeld, "Ueber die Fortpflanzung elektrodynamischer Wellen längs eines Drahtes," *Annalen der Physik*, vol. 303, no. 2, pp. 233–290, 1899. DOI: `10.1002/andp.18993030202`.

[19] F. Harms, "Elektromagnetische Wellen an einem Draht mit isolierender zylindrischer Hülle," *Annalen der Physik*, vol. 328, no. 6, pp. 44–60, 1907. DOI: `10.1002/andp.19073280603`.

[20] G. Goubau, "Surface waves and their application to transmission lines," *Journal of Applied Physics*, vol. 21, no. 11, pp. 1119–1128, 1950. DOI: `10.1063/1.1699553`.

[21] M. J. King and J. C. Wiltse, "Surface-Wave Propagation on Coated or Uncoated Metal Wires at Millimeter Wavelengths," *IRE Transactions on Antennas and Propagation*, vol. 10, no. 3, pp. 246–254, 1962. DOI: `10.1109/TAP.1962.1137859`.

[22] K. Wang and D. M. Mittleman, "Metal wires for terahertz wave guiding," *Nature*, vol. 432, no. November, pp. 376–379, Nov. 2004. DOI: `10.1038/nature03040`.

[23] D. Gacemi, A. Degiron, M. Baillergeau, and J. Mangeney, "Identification of several propagation regimes for terahertz surface waves guided by planar Goubau lines," *Applied Physics Letters*, vol. 103, no. 19, p. 1119, 2013. DOI: `10.1063/1.4829744`.

[24] J. Cabello-Sánchez, H. Rodilla, V. Drakinskiy, and J. Stake, "Transmission Loss in Coplanar Waveguide and Planar Goubau Line between 0.75 THz and 1.1 THz," in *2018 43rd International Conference on Infrared, Millimeter, and Terahertz Waves (IRMMW-THz)*, Nagoya, 2018, pp. 1–2. DOI: `10.1109/IRMMW-THz.2018.8510326`.

[25] T. Akalin and W. Padilla, "Plasmonic waveguides and metamaterial components at terahertz frequencies," *APMC 2009 - Asia Pacific Microwave Conference 2009*, pp. 2444–2446, 2009. DOI: `10.1109/APMC.2009.5385481`.

[26] L. Dazhang, J. Cunningham, M. B. Byrne, *et al.*, "On-chip terahertz Goubau-line waveguides with integrated photoconductive emitters and mode-discriminating detectors," *Applied Physics Letters*, vol. 95, no. 9, p. 092 903, Aug. 2009. DOI: `10.1063/1.3216579`.

[27] A. Treizebre, M. Hofman, and B. Bocquet, "Terahertz Spiral Planar Goubau Line Rejectors for Biological Characterization," *Progress In Electromagnetics Research M*, vol. 14, no. July, pp. 163–176, 2010. DOI: `10.2528/PIERM10072110`.

[28] W. C. Chen, J. J. Mock, D. R. Smith, D. R. Akalin, and W. J. Padilla, "Controlling Gigahertz and Terahertz Surface ElectromagneticWaves with Metamaterial Resonators," *Physical Review X*, vol. 1, no. 2, p. 021 016, Dec. 2011. DOI: `10.1103/PhysRevX.1.021016`.

[29] A. K. Horestani, W. Withayachumnankul, A. Chahadih, *et al.*, "Metamaterial-inspired bandpass filters for terahertz surface waves on goubau lines," *IEEE Transactions on Terahertz Science and Technology*, vol. 3, no. 6, pp. 851–858, 2013. DOI: `10.1109/TTHZ.2013.2285556`.

[30] Y. Xu, C. Nerguizian, and R. Bosisio, "Wideband planar Goubau line integrated circuit components at millimetre waves," *IET Microwaves, Antennas & Propagation*, vol. 5, no. 8, pp. 882–885, 2011. DOI: `10.1049/iet-map.2010.0025`.

[31] A. Treizebre, S. Laurette, Y. Xu, R. B. .-. P. I. ..., and U. 2012, "THz power divider circuits on planar Goubau lines (PGLs)," *Progress In Electromagnetics Research*, vol. 26, no. November 2011, pp. 219–228, 2012. DOI: `10.2528/PIERC11112409`.

[32] Q. Le Zhang, B. J. Chen, K. M. Shum, and C. H. Chan, "Miniaturized Spoof Surface Plasmon Polaritons Load for Planar Terahertz Circuit Application on Thick Substrate," *IEEE Transactions on Circuits and Systems II: Express Briefs*, vol. 69, no. 3, pp. 1049–1053, 2022. DOI: `10.1109/TCSII.2021.3121068`.

[33] D. Sanchez-Escuderos, M. Ferrando-Bataller, J. I. Herranz, and M. Cabedo-Fabres, "Periodic leaky-wave antenna on planar goubau line at millimeter-wave frequencies," *IEEE Antennas and Wireless Propagation Letters*, vol. 12, pp. 1006–1009, 2013. DOI: `10.1109/LAWP.2013.2278035`.

[34] Y. Pan, Y. Cheng, and Y. Dong, "Surface Plasmon Polariton Leaky-Wave Antennas with Wideband Arbitrary Multibeam Radiation," *IEEE Transactions on Antennas and Propagation*, vol. 70, no. 2, pp. 931–942, 2022. DOI: `10.1109/TAP.2021.3111210`.

[35] Q. Le Zhang, X. G. Shi, B. J. Chen, K. F. Chan, K. M. Shum, and C. H. Chan, "325 GHz to 500 GHz Single-Layer Planar Goubau- Line Antenna with Endfire Radiation Based on Substrate Mode," *IEEE Transactions on Antennas and Propagation*, no. c, pp. 1–1, 2022. DOI: `10.1109/tap.2022.3164180`.

[36] M. Swithenbank, A. D. Burnett, C. Russell, *et al.*, "On-Chip Terahertz-Frequency Measurements of Liquids," *Analytical Chemistry*, vol. 89, no. 15, pp. 7981–7987, Aug. 2017. DOI: `10.1021/acs.analchem.7b01235`.

[37] D. Debuisson, A. Treizebré, T. Houssin, *et al.*, "Nanoscale devices for online dielectric spectroscopy of biological cells," *Physiological Measurement*, vol. 29, no. 6, 2008. DOI: `10.1088/0967-3334/29/6/S19`.

[38] S. Laurette, A. Treizebre, and B. Bocquet, "Corrugated goubau lines to slow down and confine THz waves," *IEEE Transactions on Terahertz Science and Technology*, vol. 2, no. 3, pp. 340–344, 2012. DOI: `10.1109/TTHZ.2012.2189207`.

[39] S. Laurette, A. Treizebre, A. Elagli, *et al.*, "Highly sensitive terahertz spectroscopy in microsystem," *RSC Advances*, vol. 2, no. 26, p. 10 064, 2012. DOI: `10.1039/c2ra21320f`.

[40] Z. Xu, S. Li, X. Yin, H. Zhao, and L. Liu, "Radiation loss of planar surface plasmon polaritons transmission lines at microwave frequencies," *Scientific Reports*, vol. 7, no. 1, 2017. DOI: `10.1038/s41598-017-06454-y`.

[41] Q. Zhang, Q. L. Zhang, and Y. Chen, "Spoof Surface Plasmon Polariton Leaky-Wave Antennas Using Periodically Loaded Patches above PEC and AMC Ground Planes," *IEEE Antennas and Wireless Propagation Letters*, vol. 16, pp. 3014–3017, 2017. DOI: `10.1109/LAWP.2017.2758368`.

[42] Q. L. Zhang, Q. Zhang, and Y. Chen, "High-efficiency circularly polarised leakywave antenna fed by spoof surface plasmon polaritons," *IET Microwaves, Antennas and Propagation*, vol. 12, no. 10, pp. 1639–1644, 2018. DOI: `10.1049/iet-map.2017.1054`.

[43] L. Ye, W. Zhang, B. K. Ofori-Okai, *et al.*, "Super Subwavelength Guiding and Rejecting of Terahertz Spoof SPPs Enabled by Planar Plasmonic Waveguides and Notch Filters Based on Spiral-Shaped Units," *Journal of Lightwave Technology*, vol. 36, no. 20, pp. 4988–4994, 2018. DOI: `10.1109/JLT.2018.2868129`.

[44] Y. Cinar, S. Yildirim, G. Ozsahin, M. Unutmaz, and M. Unlu, "Modelling Terahertz Spoof Surface Plasmon Polariton Waveguides Using a Circuit Model," *IEEE Transactions on Terahertz Science and Technology*, vol. 11, no. 5, pp. 557–565, 2021. DOI: `10.1109/TTHZ.2021.3086690`.

[45] S. Hosseinzadeh, "A Novel Meander Sommerfeld-Goubau Line Based Sub-THz Filter," in *2022 4th West Asian Symposium on Optical and Millimeter-Wave Wireless Communications, WASOWC 2022*, IEEE, 2022, pp. 4–7. DOI: `10.1109/WASOWC54657.2022.9798420`.

[46] S. J. Park, R. Tucker, E. Pickwell-macpherson, and J. E. Cunningham, "Design of a Split Ring Resonator Integrated with On-Chip Terahertz Waveguides for Colon Cancer Detection," *Advanced Theory and Simulations*, p. 2 200 313, 2022. DOI: `10.1002/adts.202200313`.

[47] P. Overfelt, “Review of Electromagnetic Surface Waves: 1960 Through 1987,” Naval Weapons Centre, China Lake, CA, Tech. Rep., 1988.

[48] R. E. Collin, “Surface Waveguides,” in *Field Theory of Guided Waves*, vol. 30, Wiley-IEEE Press, 1991, ch. 11, pp. 697–748. DOI: `10.1109/9780470544648.ch11`.

[49] S. S. Attwood, “Surface-wave propagation over a coated plane conductor,” *Journal of Applied Physics*, vol. 22, no. 4, pp. 504–509, 1951. DOI: `10.1063/1.1699991`.

[50] W. Rotman, “A Study of Single-Surface Corrugated Guides,” *Proceedings of the IRE*, vol. 39, no. 8, pp. 952–959, 1951. DOI: `10.1109/JRPROC.1951.273719`.

[51] R. S. Elliott, “On the theory of corrugated plane surfaces,” *Transactions of the IRE Professional Group on Antennas and Propagation*, vol. 2, no. 2, pp. 71–81, 1954. DOI: `10.1109/T-AP.1954.27975`.

[52] R. A. Hurd, “The Propagation of an Electromagnetic Wave Along an Infinite Corrugated Surface,” *Canadian Journal of Physics*, vol. 32, no. 12, pp. 727–734, 1954. DOI: `10.1139/p54-079`.

[53] R. W. Hougardy and R. C. Hansen, “Scanning Surface Wave Antennas—Oblique Surface Waves Over a Corrugated Conductor,” *IRE Transactions on Antennas and Propagation*, vol. 6, no. 4, pp. 370–376, 1958. DOI: `10.1109/TAP.1958.1144619`.

[54] A. Sommerfeld, *Electrodynamics. Lectures on Theoretical Physics.* New York: Academic Press, 1952, vol. III, p. 371.

[55] J. A. Stratton, “Boundary-Value Problems,” in *Electromagnetic Theory*, 2006, pp. 524–537. DOI: `10.1002/9781119134640.ch9`.

[56] G. Goubau, “Single-Conductor Surface-Wave Transmission Lines,” *Proceedings of the IRE*, vol. 39, no. 6, pp. 619–624, 1951. DOI: `10.1109/JRPROC.1951.233782`.

[57] ——, “Waves on Interfaces,” *IRE Transactions on Antennas and Propagation*, vol. 7, no. 5, pp. 140–146, 1959. DOI: `10.1109/TAP.1959.1144747`.

[58] G. Goubau, “On the Excitation of Surface Waves,” *Proceedings of the IRE*, vol. 40, no. 7, 1952. DOI: `10.1109/JRPROC.1952.273856`.

[59] B. Vaughn and D. Peroulis, “An updated applied formulation for the Goubau transmission line,” *Journal of Applied Physics*, vol. 126, no. 19, 2019. DOI: `10.1063/1.5125141`.

[60] C. Balanis, *Antenna theory: analysis and design*, 3rd. Hoboken, New Jersey: Wiley, 2005.

[61] D. Cavallo, W. H. Syed, and A. Neto, “Equivalent Transmission Line Models for the Analysis of Edge Effects in Finite Connected and Tightly Coupled Arrays,” *IEEE Transactions on Antennas and Propagation*, vol. 65, no. 4, pp. 1788–1796, 2017. DOI: `10.1109/TAP.2017.2670616`.

[62] D. Hondros, “Über elektromagnetische Drahtwellen,” *Annalen der Physik*, vol. 335, no. 15, pp. 905–950, 1909. DOI: `10.1002/andp.19093351504`.

[63] L. W. Zelby, “Propagation modes on a dielectric coated wire,” *Journal of the Franklin Institute*, vol. 274, no. 2, pp. 85–97, Aug. 1962. DOI: `10.1016/0016-0032(62)90398-8`.

[64] J. G. Fikioris and J. A. Roumeliotis, “Cutoff Wavenumbers of Goubau Lines,” *IEEE Transactions on Microwave Theory and Techniques*, vol. 27, no. 6, pp. 570–573, 1979. DOI: `10.1109/TMTT.1979.1129673`.

[65] G. Goubau, “Open Wire Lines,” *IRE Transactions on Microwave Theory and Techniques*, vol. 4, pp. 197–200, 1956. DOI: `10.1109/TMTT.1956.1125062`.

[66] T. I. Jeon and D. Grischkowsky, “THz Zenneck surface wave (THz surface plasmon) propagation on a metal sheet,” *Applied Physics Letters*, vol. 88, no. 6, pp. 61 111–61 114, 2006. DOI: `10.1063/1.2171488`.

[67] F. Sobel, F. L. Wentworth, and J. C. Wiltse, “Quasi-Optical Surface Waveguide and Other Components for the 100- to 300-Gc Region,” *IRE Transactions on Microwave Theory and Techniques*, vol. MTT-9, no. 6, pp. 512–518, 1961. DOI: `10.1109/TMTT.1961.1125382`.

[68] Y. Xu and R. G. R. G. Bosisio, “A study of planar Goubau lines (PGLs) for millimeter- and submillimeter-wave integrated circuits (ICs),” *Microwave and Optical Technology Letters*, vol. 43, no. 4, pp. 290–293, Nov. 2004. DOI: `10.1002/mop.20448`.

[69] B. Coleman, “XXIII. Propagation of electromagnetic disturbances along a thin Wire, in a horizontally stratified medium,” *The London, Edinburgh, and Dublin Philosophical Magazine and Journal of Science*, vol. 41, no. 314, pp. 276–288, 1950. DOI: `10.1080/14786445008521797`.

[70] J. M. v. Splunter and P. M. v. d. Berg, “Spectral theory of diffraction of electromagnetic waves by a strip in the plane interface of two semi-infinite media,” *Canadian Journal of Physics*, vol. 57, no. 8, pp. 1148–1156, 1979. DOI: `10.1139/p79-161`.

[71] C. M. Butler and C. M. Butler, "Current Induced on a Conducting Strip Which Resides on the Planar Interface Between Two Semi-Infinite Half-Spaces," *IEEE Transactions on Antennas and Propagation*, vol. 32, no. 3, pp. 226–231, 1984. DOI: `10.1109/TAP.1984.1143308`.

[72] C. I. Hsu, R. F. Harrington, K. A. Michalski, and D. Zheng, "Analysis of multiconductor transmission lines of arbitrary cross section in multilayered uniaxial media," *IEEE Transactions on Microwave Theory and Techniques*, vol. 41, no. 1, pp. 70–78, 1993. DOI: `10.1109/22.210231`.

[73] M. Friedman and R. F. Fernsler, "Guiding radio frequency waves on metallic foils," *Applied Physics Letters*, vol. 74, no. 23, pp. 3468–3470, 1999. DOI: `10.1063/1.124130`.

[74] W. Hong and Y. D. Lin, "Single-conductor strip leaky-wave antenna," *IEEE Transactions on Antennas and Propagation*, vol. 52, no. 7, pp. 1783–1789, 2004. DOI: `10.1109/TAP.2004.829854`.

[75] A. Treizebré, T. Akalin, and B. Bocquet, "Planar excitation of goubau transmission lines for THz BioMEMS," *IEEE Microwave and Wireless Components Letters*, vol. 15, no. 12, pp. 886–888, 2005. DOI: `10.1109/LMWC.2005.859976`.

[76] A. Treizebré, B. Bocquet, Y. Xu, and R. G. Bosisio, "New THz excitation of planar Goubau line," *Microwave and Optical Technology Letters*, vol. 50, no. 11, pp. 2998–3001, Nov. 2008. DOI: `10.1002/mop.23850`.

[77] A. Gopinath, "Losses in Coplanar Waveguides," *IEEE Transactions on Microwave Theory and Techniques*, vol. 30, no. 7, pp. 1101–1104, 1982. DOI: `10.1109/TMTT.1982.1131204`.

[78] K. Koshiji, E. Shu, and S. Miki, "Dielectric and conductor losses in coplanar waveguides," *Electronics and Communications in Japan (Part I: Communications)*, vol. 65, no. 12, pp. 55–64, 1982. DOI: `10.1002/ecja.4400651208`.

[79] Y. C. Shih and T. Itoh, "Analysis of conductor-backed coplanar waveguide," *Electronics Letters*, vol. 18, no. 12, pp. 440–538, 1982. DOI: `10.1049/el:19820365`.

[80] S. B. Cohn, "Slot Line on a Dielectric Substrate," *IEEE Transactions on Microwave Theory and Techniques*, vol. 17, no. 10, pp. 768–778, 1969. DOI: `10.1109/TMTT.1969.1127058`.

[81] G. Kirchhoff, " LIV. On the motion of electricity in wires," *The London, Edinburgh, and Dublin Philosophical Magazine and Journal of Science*, vol. 13, no. 88, pp. 393–412, 1857. DOI: `10.1080/14786445708642318`.

[82] O. Heaviside, " XIX. On the extra current," *The London, Edinburgh, and Dublin Philosophical Magazine and Journal of Science*, vol. 2, no. 9, pp. 135–145, 1876. DOI: `10.1080/14786447608639176`.

[83] R. E. Collin, "Waves on a Lossy Transmission Line," in *Foundations for Microwave Engineering*, 2nd, Hoboken, New Jersey: Wiley InterScience, 2001, ch. 3, pp. 86–89. DOI: `10.1109/9780470544662.ch3`.

[84] R. Marks and D. Williams, "A general waveguide circuit theory," *Journal of Research of the National Institute of Standards and Technology*, vol. 97, no. 5, pp. 533–562, 1992. DOI: `10.6028/jres.097.024`.

[85] S. A. Schelkunoff, "Impedance concept in wave guides," *Quarterly of Applied Mathematics*, vol. II, pp. 1–15, 1944. DOI: `10.1090/qam/11833`.

[86] T. E. Roberts, "Theory of the single-wire transmission line," *Journal of Applied Physics*, vol. 24, no. 1, pp. 57–67, 1953. DOI: `10.1063/1.1721134`.

[87] D. B. Rutledge, S. E. Schwarz, and A. T. Adams, "Infrared and submillimetre antennas," *Infrared Physics*, vol. 18, no. 5-6, pp. 713–729, 1978. DOI: `10.1016/0020-0891(78)90094-5`.

[88] F. Monticone and A. Alù, "Leaky-wave theory, techniques, and applications: From microwaves to visible frequencies," *Proceedings of the IEEE*, vol. 103, no. 5, pp. 793–821, 2015. DOI: `10.1109/JPROC.2015.2399419`.

[89] A. A. Oliner and H. Shigesawa, "New Interesting Leakage Behavior on Coplanar Waveguides of Finite and Infinite Widths," *IEEE Transactions on Microwave Theory and Techniques*, vol. 39, no. 12, pp. 2130–2137, 1991. DOI: `10.1109/22.106555`.

[90] L. Hatkin, "Analysis of Propagating Modes in Dielectric Sheets," *Proceedings of the IRE*, vol. 42, no. 10, pp. 1565–1568, 1954. DOI: `10.1109/JRPROC.1954.274764`.

[91] M. Riaziat, R. Majidi-Ahy, and I. J. Feng, "Propagation Modes and Dispersion Characteristics of Coplanar Waveguides," *IEEE Transactions on Microwave Theory and Techniques*, vol. 38, no. 3, pp. 245–251, 1990. DOI: `10.1109/22.45333`.

[92] K. Mizuno, S. Ono, and Y. Daiku, "Design of Printed Resonant Antennas for Monolithic-Diode Detectors," *IEEE Transactions on Microwave Theory and Techniques*, vol. 25, no. 6, pp. 470–472, 1977. DOI: `10.1109/TMTT.1977.1129136`.

[93] S. J. Orfanidis, *Electromagnetic Waves and Antennas*, Rutgers U. 2002, vol. 2, pp. 313–321. DOI: `10.1016/B978-075064947-6/50011-3`.

[94] D. R. Jackson, F. Mesa, M. J. Freire, D. P. Nyquist, and C. Di Nallo, “Excitation theory for bound modes, leaky modes, and residual-wave currents on stripline structures,” *Radio Science*, vol. 35, no. 2, pp. 495–510, 2000. DOI: `10.1029/1999RS900076`.

[95] D. Grischkowsky, I. N. Duling, J. C. Chen, and C. C. Chi, “Electromagnetic shock waves from transmission lines,” *Physical Review Letters*, vol. 59, no. 15, pp. 1663–1666, Oct. 1987. DOI: `10.1103/PhysRevLett.59.1663`.

[96] D. B. Rutledge, D. P. Neikirk, and D. P. Kasilingam, “Integrated-Circuit Antennas,” in *Infrared and millimeter waves*, vol. 10, New York: Academic, 1983, ch. 1, pp. 1–62.

[97] ——, “Integrated-Circuit Antennas,” in *Infrared and millimeter waves*, New York: Academic, 1983, ch. 1, pp. 59–63.

[98] A. F. Harvey, “Periodic and Guiding Structures at Microwave Frequencies,” *IRE Transactions on Microwave Theory and Techniques*, vol. 8, no. 1, pp. 30–61, 1960. DOI: `10.1109/TMTT.1960.1124658`.

[99] R. E. Collin, “Periodic Structures and Filters,” in *Foundations for Microwave Engineering*, 2nd, Hoboken, New Jersey: Wiley InterScience, 2001, ch. 8, pp. 550–647. DOI: `10.1109/9780470544662.ch8`.

[100] ——, “Surface Waves Along a Corrugated Plane,” in *Field Theory of Guided Waves*, Wiley-IEEE Press, 1991, ch. 11.4, pp. 708–712. DOI: `10.1109/9780470544648.ch11`.

[101] J. Cabello-Sanchez, V. Drakinskiy, J. Stake, and H. Rodilla, “A corrugated planar-Goubau-line termination for terahertz waves,” *arXiv preprint*, 2022.

[102] S. A. Maier, S. R. Andrews, L. Martín-Moreno, and F. J. García-Vidal, “Terahertz surface plasmon-polariton propagation and focusing on periodically corrugated metal wires,” *Physical Review Letters*, vol. 97, no. 17, pp. 1–4, 2006. DOI: `10.1103/PhysRevLett.97.176805`.

[103] T. Weiland, “Discretization Method for the Solution of Maxwell’s Equations for Six-Component Fields.,” *AEU-Archiv fur Elektronik und Ubertragungstechnik*, vol. 31, no. 3, pp. 116–120, 1977.

[104] J. H. Coggon, “Classic Paper. Electromagnetic and electrical modeling by the finite element method.,” *Geophysics*, vol. 36, no. 1, pp. 132–155, 1971. DOI: `10.1190/1.1440151`.

[105] N. Fuse, T. Takahashi, Y. Ohki, R. Sato, M. Mizuno, and K. Fukunaga, "Terahertz Spectroscopy as a New Tool for Insulating Material Analysis and Condition Monitoring," *IEEE Insulating Magazine*, vol. 27, no. 3, pp. 26–35, 2011. DOI: `10.1109/MEI.2011.5871366`.

[106] J. Dai, J. Zhang, W. Zhang, and D. Grischkowsky, "Terahertz time-domain spectroscopy characterization of the far-infrared absorption and index of refraction of high-resistivity, float-zone silicon," *Journal of the Optical Society of America B*, vol. 21, no. 7, p. 1379, 2004. DOI: `10.1364/JOSAB.21.001379`.

[107] M. Y. Frankel, S. Gupta, J. A. Valdmanis, and G. A. Mourou, "Terahertz Attenuation and Dispersion Characteristics of Coplanar Transmission Lines," *IEEE Transactions on Microwave Theory and Techniques*, vol. 39, no. 6, pp. 910–916, 1991. DOI: `10.1109/22.81658`.

[108] M. F. Bauwens, N. Alijabbari, A. W. Lichtenberger, N. S. Barker, and R. M. Weikle, "A 1.1 THz micromachined on-wafer probe," in *2014 IEEE MTT-S International Microwave Symposium (IMS2014)*, Tampa, FL, 2014, pp. 1–4. DOI: `10.1109/MWSYM.2014.6848607`.

[109] Jingjing, S. Alexandrou, and T. Hsiang, "Attenuation characteristics of coplanar waveguides at subterahertz frequencies," *IEEE Transactions on Microwave Theory and Techniques*, vol. 53, no. 11, pp. 3281–3287, Nov. 2005. DOI: `10.1163/156939306779276767`.

[110] M. Spirito, U. Arz, G. N. Phung, F. J. Schmückle, W. Heinrich, and R. Lozar, *Guidelines for the design of calibration substrates, including the suppression of parasitic modes for frequencies up to and including 325 GHz: EMPIR 14IND02-PlanarCal*, 2018. DOI: `10.7795/530.20190424A`.

[111] D. J. Segelstein, "The complex refractive index of water," Ph.D. dissertation, Department of Physics, University of Missouri–Kansas City, 1981, p. 167.

[112] J. T. Kindt and C. A. Schmuttenmaer, "Far-Infrared Dielectric Properties of Polar Liquids Probed by Femtosecond Terahertz Pulse Spectroscopy," *The Journal of Physical Chemistry*, 1996. DOI: `10.1021/jp960141g`.

[113] J. Kitagawa, T. Ohkubo, M. Onuma, and Y. Kadoya, "THz spectroscopic characterization of biomolecule/water systems by compact sensor chips," *Applied Physics Letters*, vol. 89, no. 4, p. 41 114, 2006. DOI: `10.1063/1.2236295`.

[114] J. N. Lee, C. Park, and G. M. Whitesides, “Solvent Compatibility of Poly(dimethylsiloxane)-Based Microfluidic Devices,” *Analytical Chemistry*, vol. 75, no. 23, pp. 6544–6554, 2003. DOI: `10.1021/ac0346712`.